Anisotropic scintillation indices for weak scattering regime

D. Vasylyev[1], Y. Béniguel[2], V. Wilken[1], M. Kriegel[1], and J. Berdermann[1]

[1]Institute for Solar-Terrestrial Physics, German Aerospace Center, Neustrelitz, Germany
[2]Informatique Electromagnétisme Electronique Analyse Numérique (IEEA), Courbevoie/Paris, France

Key Points:

- Analytic expressions for amplitude and phase scintillation indices are derived accounting effects connected with the finite curvature of the Earth and of the ionospheric shell.
- Geometric enhancement of scintillation is connected to the relative position of the communication link and of the anisotropic ionospheric irregularity.
- Depending on the use case the obtained results are expressed either in geographical or local coordinates of sending or receiving stations.

Corresponding author: D. Vasylyev, dmytro.vasylyev@dlr.de

Abstract

Transionospheric radio signals might undergo random modulations of their amplitude and phase caused by scattering on irregular structures in the ionosphere. This phenomenon, known as scintillation, is governed by the space weather conditions, time of the day, season, local distribution of the geomagnetic field, etc. All these factors make ionospheric scintillation both highly variable in space and time. Moreover, scintillation are intrinsically anisotropic since the associated scattering irregularities tend to align and stretch along the geomagnetic field lines. Depending on the relative position of signal source, the receiving station, and the irregularity, the scintillation effect on the transmitted wave might be enhanced or reduced. This study is focused on the consistent accounting of this geometric effect in scintillation modeling with the emphasis on situations when the communication or sensing sender-receiver link is nearly horizontal. For this task the single phase screen model has been used to model the scattering of propagating radio signals on random ionospheric layer. The geometric enhancement effect of scintillation is demonstrated by considering communication links via a geostationary beacon satellite over the equator.

1 Introduction

Atmospheric scintillation phenomena are versatile on their physical origin and wide in the spectrum of electromagnetic frequencies for signals that are affected. The most prominent example of optical scintillation is the twinkling and shimmering of stars. These effects are associated with the turbulent tropospheric flows that create random gradients of the atmospheric refraction index. The optical or infrared radiation propagating through such a random refractive medium exhibits fluctuations of intensity and phase when reaching the ground-based observer. Similar disturbing effects might affect the performance of remote-sensing and communication satellites, free space optical communication terminals, lidars, military thermal infrared imaging systems, to name just a few.

For radio wave remote sensing and communication applications the ionospheric scintillation phenomena are predominantly responsible for a random degradation of the received signal. This kind of signal disturbances affects the performance of retrieval algorithms and reduces the margins of the reliable information transfer. The records of astronomical radio sources might be deteriorated by the disturbed ionosphere in a similar manner as the optical images of the stars are affected by the tropospheric turbulence. Ionospheric scintillation might also devastatingly impact current and future life-critical systems that are based on positioning services, such as the Ground-Based Augmentation System (GBAS), nautical navigation, autonomous driving, etc.

Similarly to tropospheric scintillation the ionospheric ones are related to the random variations of the refractive properties of the medium, i.e. of the ionospheric plasma. Due to the high variability of the random plasma and due to the complexity of nonlinear processes and instabilities responsible for the formation of plasma vortices and blobs of different sizes and shapes, the irregular ionospheric medium is treated statistically. The statistical properties of the random plasma is very similar to the corresponding properties of the turbulent air.The peculiar feature of ionospheric scintillation, however, is its spatial anisotropy. This feature arises mainly due to the tendency of ionospheric irregular structures to stretch and align along the geomagnetic lines of force.

The need for accounting for the anisotropy effects in the theory and modeling of ionospheric scintillation was recognized quite early (Spencer, 1955; Booker, 1956). It was inspired by the observation of anisotropic diffraction patterns formed on the ground by distant radio sources and reconstructed via the correlation analysis (Briggs et al., 1950; Wild & Roberts, 1955; Ratcliffe, 1956). Such patterns are of nearly elliptic shapes that suggested that inhomogeneities forming these diffraction footprints could be represented by ellipsoidal isosurfaces of deviations of plasma refraction index from the values of the

ambient ionosphere. The convenient coordinate system associated with the orientation of the ellipsoidal surfaces have been introduced in (Briggs & Parkin, 1963) and generalized in (Singleton, 1970). Particularly, the Singleton coordinates are suitable for field-aligned irregularities, for which one semi-major axis of the characteristic ellipsoid is aligned along the geomagnetic lines of force.

If the records of random fades in radio signals undergo correlation analysis at the same spatial point, one obtains an important statistical characteristics of the signal disturbance. Due to the high variability of signal fades, the time averages of the resulting statistical quantities, known as scintillation indices, are considered over some predefined time period. Depending on whether phase or amplitude fades are of interest the respective scintillation indices are derived from the received signal. The phase scintillation index then characterizes how strong the phase front of the signal wave is corrugated while propagating through ionospheric irregularities. The amplitude scintillation index characterizes random modulation of the received power due to signal scattering on random ionospheric structures.

The anisotropy of irregularities that cause phase and amplitude disturbances affects the scintillation phenomena as well. The resulting scintillation indices are also spatially anisotropic. For example the level of amplitude scintillation increases as the axial ratio of characteristic ellipsoid of ionospheric irregularities increases (Kumagai & Ogawa, 1986; Gola et al., 1992; Anderson & Straus, 2005; Jandieri et al., 2017). Similarly, the phase scintillation is enhanced if the ray trajectory of the signal orients most closely to the geomagnetic field line (Prikryl et al., 2011; Afraimovich et al., 2011; Bezler et al., 2019; Hong et al., 2020; Yang et al., 2020). These geometric enhancement effects of ionospheric scintillations could be also masked or contaminated by other effects such as due to the multipath contributions received at small elevation angles (Atilaw et al., 2017).

In connection with the GNSS-assisted positioning and navigation services the proper accounting for the geometry-related effects in the scintillation-related disturbances is of importance. This is because the improvement in positioning accuracy is related to the usage of carrier-phase measurements of the modern GNSS receivers. That makes the precise positioning services to be sensitive to ionospheric scintillation and to its anisotropy (Banville & Langley, 2013; Prikryl et al., 2016; Linty et al., 2018; Yang et al., 2020). The proper modeling of scintillation at low elevation angles is also important for distinguishing ionospheric scintillation from the multipath in GNSS signals (C. Li et al., 2022).

Remote sensing via the radio occultation methods might also be affected by scintillation. Moderate and strong scintillation contribute to significant errors in the neutral bending angle measurements (Yakovlev et al., 1995; Ludwig−Barbosa et al., 2020). Thus accounting for the geometry of scintillation-causing irregularities is important to increase in accuracy of occultation measurements near the equator during periods of high scintillation activity (Anderson & Straus, 2005)

In GNSS reflectometric remote sensing applications, the amplitude scintillation and range errors also contribute the most to degradation of the retrieved signals. This is due to the peculiarity of the data processing (Camps et al., 2016). At the same time, in some reflectometric measurements the retrieval is optimal at low elevation angles (Semmling et al., 2014; Dielacher et al., 2022) and the consistent inclusion of geometric effects in the modeling of amplitude scintillation affecting possible observation events is of a great importance.

The imaging and interferometric applications via SAR satellites are affected by small-scale ionospheric structures as well. Amplitude and phase fluctuations reduce the effective resolution of a SAR image (Xu et al., 2004; Ji et al., 2020), may lead to the striping artifacts and image defocusing (Meyer et al., 2016; Sato et al., 2021), to the decorrelation effects, and to the interferometric phase errors (Y. Li et al., 2018). The orien-

tation of the scintillation-causing irregularities in space relative to the SAR beam should be accounted for the efficient mitigation of these negative effects on image formation (Carrano et al., 2012; Mohanty et al., 2019).

The theoretical treatment of anisotropic scintillation based on the model of a single phase screen have been developed in Refs. (Rino & Fremouw, 1977; Rino, 1979a, 1979b). The anisotropy effect is incorporated in this theory by considering the correlation function of electron density fluctuations for scintillation-causing irregularities. The correlation isosurfaces are taken to be of ellipsoidal form. This correlation function (or, alternatively, its spectral representation – the power spectral density) is used for the generation of a phase screen that possesses similar statistical characteristics as the bulk layer of the scintillation-associated irregular ionosphere. The phase screen, placed along the propagation path of the signal wave, acts as a random lens that can focus some parts of the wave while defocus other ones. The wave front of the wave emanating from this phase screen is corrugated. The phase of the disturbed wave exhibits random spatial and temporal fluctuations, i.e., it scintillates. On the other hand, the constructive and destructive interference of parts of initial wave that has been focused or defocused would show amplitude scintillations, the level of which would be maximized if the observation plane is placed at certain distance from the phase screen, known as the Fresnel distance.

In the weak scattering regime, i.e., when the focusing and defocusing effects of the screen are considered to be weak, (Rino, 1979a) was able to obtain the analytic formulas for the scintillation indices. This theory became later the base for the global climatological scintillation model WBMOD (Secan & Fremouw, 1983; Secan et al., 1995, 1997) and has been validated in multiple studies (Knight et al., 1999; Cervera et al., 2001; Forte & Radicella, 2005; Priyadarshi & Wernik, 2013; Carter et al., 2014). One of the premises of this theoretical treatment is the assumption that the source of the radio signal is positioned in near vertical direction to the ground-based receiver. In this approximation the effects connected to the finite curvature of the ionospheric layer can be neglected, while the slant signal propagation paths are treated via the series of suitable projection transformations. As an example of such transformations, the vertical distances are projected to the slant ones via the multiplication on the mapping function $\sec\theta$, where θ is the observer zenith angle. It is clear that at the zenith angles close to $\pi/2$ radians the secant function diverges and yields the inadequate values for the slant ranges. In fact, for the very slant links the inclusion of effects connected with the finite curvature of the earth and of the ionospheric layer is necessary.

To our knowledge the first attempt to include the corrections to the classical theory of (Rino, 1979a, 1979b) in order to make it applicable for very slant propagation paths has been undertaken in Ref. (Priyadarshi & Wernik, 2013). Priyadarshi and Wernik performed the qualitative analysis of scintillation indices and treated their divergency for slant links by the appropriate replacement of the satellite elevation angle by the elevation angle of the observer (El-Arini et al., 1994). Still, the functional dependence of the scintillation indices on the elevation angle in this work has been adapted from the original flat-geometry formulation (Rino, 1979a) and thus the proposed modification is not fully consistent generalization to the spherical geometry. In Ref. (Vasylyev et al., 2022) we considered the geometric aspects of the scintillation modeling in more consecutive manner and listed the expressions for the scintillation indices in the weak scattering regime assuming the sphericity of the ionospheric shell. The present article provides more details on this treatment of the radio wave propagation in a weakly scattering random medium with the inclusion of spherical geometry of the ionospheric layer and of the Earth surface.

The article is structured as follows. In section 2 the general formulation of the problem of electromagnetic wave propagation in the random ionosphere is formulated. In the case of weak scattering the solution of this problem can be provided by using the model a thin random phase screen as outlined in Sec. 3. The anisotropy of scintillation-causing

irregularities is considered in Sec. 4 and the resulting scintillation indices are discussed in Sec. 5. In Sec. 6 the geometric enhancement of scintillation is demonstrated for the vertical and slant signal propagation links. Finally, some concluding remarks are summarized in Sec. 7.

2 Wave Propagation in a Randomly Inhomogeneous Ionosphere

In the following we will deal with the radiofrequency signal formed on the sender site. Let us assume that the sender antenna radiates in the direction towards the receiver. Also it spatially limits the signal wave in the directions transversal to the propagation direction. Thus, the signal wave has a beam shape. If the radiate field remains confined to a narrow cone of propagation angles, its transmission through a randomly disturbed ionosphere can be approximately described by the scalar parabolic equation for a function $u(\boldsymbol{r})$ of the spatial coordinate $\boldsymbol{r}$. Provided the depolarization effect of the ionosphere on propagating electromagnetic wave is negligibly small (Kravtsov, 1970; Crane, 1977), the function $u(\boldsymbol{r})$ can be related to one of the components of the electric field. Without loss of generality we consider the linearly polarized wave with the component E_p of the electric field along the polarization direction p and write

$$E_p(\boldsymbol{r}) = u(\boldsymbol{r})e^{i(kz-\omega t)}. \tag{1}$$

Here the coordinate system is chosen such that its center locates at the center of irregularity of characteristic size ℓ along the vertical and the z-axis is collinear to the propagation direction, $k = (\omega/c)(\langle\varepsilon\rangle/\varepsilon_0)$ is the wavenumber, ω is the wave angular frequency, c is the speed of light, $\langle\varepsilon\rangle$ is the average dielectric permittivity of the ionospheric medium, and ε_0 is the vacuum permittivity. The equation for $u(\boldsymbol{r})$ reads as

$$2ik\,\frac{\partial u(\boldsymbol{r})}{\partial z} + \Delta_\perp u(\boldsymbol{r}) + 2k^2\delta n(\boldsymbol{r})u(\boldsymbol{r}) = 0, \tag{2}$$

where $\Delta_\perp = \partial^2/\partial x^2 + \partial^2/\partial y^2$ is the transverse Laplace operator. The absence of the second-order derivative with respect to z in Eq. (2) is connected with the assumption that the wave is mainly scattered in the forward direction, that corresponds to the condition $\langle\delta n^2\rangle z/\ell \ll 1$. If we assume that the plasma is collisionless, then the fluctuating part of the refractive index is related to the fluctuating part of the electron density δN_e as

$$\delta n(\boldsymbol{r}) \approx \frac{1}{2}\frac{\varepsilon(\boldsymbol{r}) - \langle\varepsilon\rangle}{\langle\varepsilon\rangle} = -\frac{1}{2}\frac{(\omega_p/\omega)^2}{1-(\omega_p/\omega)^2}\frac{\delta N_e(\boldsymbol{r})}{\langle N_e\rangle}, \tag{3}$$

where $\omega_p^2 = e^2\langle N_e\rangle/(\varepsilon_0 m)$ is the squared plasma frequency, $\langle N_e\rangle$ is the ambient electron density, e is the elementary charge, and m is the electron mass. For the electromagnetic waves with frequencies much larger that the plasma frequency (i.e., larger than 1-1.5 MHz) Eq. (3) can be written as

$$\delta n(\boldsymbol{r}) \approx -\frac{r_e\lambda^2}{2\pi}\delta N_e(\boldsymbol{r}), \tag{4}$$

where $r_e \approx 2.818\times10^{-15}$ m is the classical electron radius and $\lambda = 2\pi c/\omega$ is the wavelength of the electromagnetic wave. We use this high-frequency assumption in the following and note that it also implies that $k \approx \omega/c$, i.e., the value of the wave number in medium is approximately equal to its value in the vacuum.

The equation (2) establishes the relationship between the random wave u and the random function δn. In the view of stochastic nature of the function $u(\boldsymbol{r})$, the properties of the transmitted wave are characterized by the moments of u or by their combinations. One such a combination that is widely used is the intensity or amplitude scintillation index

$$S_4 = \sqrt{\frac{\langle I^2\rangle - \langle I\rangle^2}{\langle I\rangle^2}}, \tag{5}$$

where $I = |E_p|^2 = |u|^2$ is the intensity of the transmitted wave. The index S_4, as seen from its definition, characterizes the strength of intensity deviations from the mean intensity.

The amplitude scintillation index as defined in Eq. (5) uses the absolute values of the electric field. However, in some applications the information on the strength of phase fluctuations is of higher importance. Denoting the phase departure of the wave detected by the observer as S the index

$$\sigma_S = \sqrt{\langle S^2 \rangle - \langle S \rangle^2} \tag{6}$$

characterizes the strength of phase fluctuations from the mean phase value. Since the phase is a circular variable, this definition is applicable as statistical measure if the phase deviations from the mean are less than the value of π.

3 Thin Phase Screen Approximation

One method for solving Eq. (2) is based on the assumption that the irregular medium is being thin enough and the diffraction-associated spreading of the wave propagating within this medium is thus negligible. This requirement is met if the corresponding r.m.s. angle of scatter is negligibly small, i.e., $1/kl_0 \ll 1$, with l_0 being the typical scale size of ionospheric irregularities contributing to the diffraction-associated scattering [inner-scale parameter in Ref. (Yeh & Liu, 1982)]. In this case we can neglect the term $\Delta_\perp u$ in (2), cf. Ref. (Uscinski, 1977), and solve the resulting equation taking the plane wave of constant amplitude U_0 to be the associated boundary condition. The solution for this part of propagation in the medium reads as

$$u_0(\boldsymbol{r}_\perp) = U_0\, e^{i\,\delta\varphi(\boldsymbol{r}_\perp)}, \tag{7}$$

where $\boldsymbol{r}_\perp = (x \quad y)^T$ is the transverse component of position vector $\boldsymbol{r}$ and

$$\delta\varphi(\boldsymbol{r}_\perp) = k \int_0^s \delta n(\boldsymbol{r}) \mathrm{d}z = -r_e \lambda \int_0^s \delta N_e(\boldsymbol{r}) \mathrm{d}z \tag{8}$$

is the phase increment gained by propagation through a thin slab of random medium. In general, the integration in Eq. (8) is along the slant distance from the screen and the receiver defined in Eq. (A15) of Appendix A or in Eq. (C7) of Appendix C. We also note that since the ionosphere has a finite thickness and δN_e is zero at some distance Δs, the limits of integration in Eq. (8) can be restricted to the interval $[0, \Delta s]$.

Equation (7) shows that the propagation in the medium reduces to the random phase modulation of the incoming wave if one neglects the diffraction effects associated with the term $\Delta_\perp u$. This result corresponds to the model of a thin phase-changing irregular screen (Booker et al., 1950; Hewish, 1951; Briggs & Parkin, 1963; Rino, 1979a). In the phase screen approach the result (7) is used further as the boundary condition for the parabolic equation (2) where the term proportional to δn is omitted. The solution of this equation, namely

$$u(\boldsymbol{r}) = u(\boldsymbol{r}_\perp, z) = \frac{ikU_0}{2\pi z} \int e^{-i\left(\delta\varphi(\boldsymbol{r}'_\perp) + \frac{k}{2z}|\boldsymbol{r}_\perp - \boldsymbol{r}'_\perp|^2\right)} \mathrm{d}^2\boldsymbol{r}_\perp, \tag{9}$$

describes the propagation in free-space along the path from the lower boundary of irregular medium to the receiver. Since the length of this path is sufficiently large the diffraction-associated broadening cannot be neglected as it was done by derivation of Eq. (7).

By choosing $z{=}s$, i.e., considering the transmitted wave at the receiver, the solution $u(\boldsymbol{r}_\perp, s)$ can be used for the calculation of the scintillation indices (5), (6). To this end we can formally write the solution (9) as

$$u(\boldsymbol{r}_\perp, s) = U_0 \exp\left[\chi(\boldsymbol{r}_\perp, s) - iS(\boldsymbol{r}_\perp, s)\right], \tag{10}$$

where

$$\chi(\boldsymbol{r}) = \log \frac{|u(\boldsymbol{r})|}{U_0} \tag{11}$$

is the log-amplitude of the wave and S is its phase departure.

It is quite natural to consider $\delta\varphi$ to be a Gaussian random field with the zero mean assuming that the conditions of the central limiting theorem is applicable for these random phase increments[1] (De Wolf, 1974). If the phase excursions are small, i.e., $\langle\delta\varphi^2\rangle \ll 1$, we may expand the exponent $\exp(-i\delta\varphi)$ in Eq. (9) into series and retain the terms of order $O(\delta\varphi)$ only. Similarly, we expand the exponent in Eq. (10) up to the corresponding order. This allows us to express the log-amplitude and phase departure in terms of $\delta\varphi$ as (Wernik et al., 1983)

$$\chi(\boldsymbol{r}_\perp, z) = \frac{k}{2\pi z}\int \delta\varphi(\boldsymbol{r}'_\perp)\,\cos\Big(\frac{k}{2z}|\boldsymbol{r}_\perp - \boldsymbol{r}'_\perp|^2\Big)\mathrm{d}^2\boldsymbol{r}'_\perp, \tag{12}$$

$$S(\boldsymbol{r}_\perp, z) = \frac{k}{2\pi z}\int \delta\varphi(\boldsymbol{r}'_\perp)\,\sin\Big(\frac{k}{2z}|\boldsymbol{r}_\perp - \boldsymbol{r}'_\perp|^2\Big)\mathrm{d}^2\boldsymbol{r}'_\perp. \tag{13}$$

These expressions are used for obtaining the moments of χ and S that, in turn, allows one to calculate the scintillation indices (5) and (6).

Consider the (auto)correlation functions for the random fields $X = \chi, S$ defined as

$$\rho_X(\mathbf{r}_1, \mathbf{r}_2) = \langle[X(\mathbf{r}_1) - \langle X(\mathbf{r}_1)\rangle][X(\mathbf{r}_2) - \langle X(\mathbf{r}_2)\rangle]\rangle \equiv \langle X(\mathbf{r}_1)X(\mathbf{r}_2)\rangle, \tag{14}$$

where we have used $\langle\chi\rangle$=$\langle S\rangle$=0 as the consequence of $\langle\delta\varphi\rangle$=0. In the following we assume the spatial homogeneity of the random fields that implies $\rho_X(\mathbf{r}_1, \mathbf{r}_2) = \rho_X(\mathbf{r}_1 - \mathbf{r}_2)$. The correlation function is related to the power spectral density (PSD) of the random field X via the Fourier transform

$$\Phi_X(\boldsymbol{\kappa}) = \int \rho_X(\boldsymbol{r}) e^{-i\boldsymbol{\kappa}\cdot\boldsymbol{r}}\frac{\mathrm{d}^3\boldsymbol{r}}{(2\pi)^3} = \int \rho_X(\boldsymbol{r})\cos(\boldsymbol{\kappa}\cdot\boldsymbol{r})\frac{\mathrm{d}^3\boldsymbol{r}}{(2\pi)^3}. \tag{15}$$

Both the correlation and PSD functions provide the basic information on the statistical properties of random fields.

Substituting Eqs. (12) and (13) in (14) one can express the correlation functions of the log-amplitude and phase fluctuations in terms of the PSD of the screens phase increment, $\Phi_{\delta\varphi}$, as (Yeh & Liu, 1982):

$$\rho_\chi(\boldsymbol{r}_\perp, s) = \int \Phi_{\delta\varphi}(\boldsymbol{\kappa}_\perp)\sin^2\Big(\frac{s}{2k}\kappa_\perp^2\Big)\cos(\boldsymbol{\kappa}_\perp\cdot\boldsymbol{r}_\perp)\mathrm{d}^2\boldsymbol{\kappa}_\perp, \tag{16}$$

$$\rho_S(\boldsymbol{r}_\perp, s) = \int \Phi_{\delta\varphi}(\boldsymbol{\kappa}_\perp)\cos^2\Big(\frac{s}{2k}\kappa_\perp^2\Big)\cos(\boldsymbol{\kappa}_\perp\cdot\boldsymbol{r}_\perp)\mathrm{d}^2\boldsymbol{\kappa}_\perp. \tag{17}$$

These expressions determine the correlation functions in the plane transversal to the propagation direction and placed at a distance s from the phase screen. From the operational point of view, the plane, in which correlation analysis is performed, is taken to be the tangent to the Earth surface at the receiver location. Adaptation of Eqs. (16), (17) to such measurement geometry is considered in Appendix B. For our further analysis we would be interested in autocorrelation of values measured in the same spatial point $\boldsymbol{r}_\perp$=0, so we can use Eqs. (16), (17) without any additional adjustment to the coordinate system of the receiver.

[1] Strictly speaking, the phase is a circular variable and the limiting theorem is formulated in terms of $\cos\delta\varphi$ and $\sin\delta\varphi$. However as far as $\langle\delta\varphi^2\rangle \ll 1$ the assumption that $\delta\varphi$ is distributed normally with the zero mean and the variance $\sqrt{\langle\delta\varphi^2\rangle}$ is well justified.

Since the phase screen random modulation function $\delta\varphi$ is defined as a model variable, it should be connected to the empirical quantity characterizing the random ionosphere, such as the electron density fluctuation δN_e. We now assume that a region of the random irregular electron density is bounded within the spherical shell with the radii $R_\oplus + h_p$ and $R_\oplus + h_p - \Delta h$, where $R_\oplus$ is the Earth radius, h_p is the altitude of the phase screen, and Δh is the thickness of the shell. We also assume that the random ionospheric medium is spatially homogeneous within this shell. Then, by using the relationship (8) one obtains[2]

$$\Phi_{\delta\varphi}(\boldsymbol{\kappa}_\perp) = 2\pi\Delta s\lambda^2 r_e^2 \Phi_{\delta N_e}(\boldsymbol{\kappa}_\perp, 0), \tag{18}$$

where $\Delta s = \Delta h \cdot M$ is the slant thickness of the shell with M being the vertical-to-slant mapping function, which explicit form is derived in Appendix C. The expression (18) relates the two-dimensional model spectrum for phase increment and the three-dimensional spectrum of electron density fluctuations. The latter can be obtained experimentally by means of correlation analysis of electron density fluctuations and exhibits the power-law dependence on the spatial frequency $\boldsymbol{\kappa}$. Such dependence can be modeled by the von Karman function (von Karman, 1948; Vasylyev et al., 2022)

$$\Phi_{\delta N_e}(\boldsymbol{\kappa}) = \frac{\langle \delta N_e^2 \rangle}{\pi^{3/2}} \frac{\Gamma\left(\frac{p+2}{2}\right)}{\Gamma\left(\frac{p-1}{2}\right)} \frac{\kappa_0^{p-1}}{\left(\kappa^2 + \kappa_0^2\right)^{\frac{p+2}{2}}} \tag{19}$$

defined in the spatial frequency range $\kappa_0 \ll \kappa \ll \kappa_m$ with κ_0 is associated with the largest spatial scale of random ionospheric inhomogeneities, while κ_m is associated with the inner-scale l_0 of the random ionosphere. Here $\langle \delta N_e^2 \rangle$ is the variance of the electron density fluctuations, p is the (one-dimensional) spectral index and $\Gamma(x)$ is the gamma function. The model parameters $\langle \delta N_e^2 \rangle$, κ_0, and p can be inferred from the empirical spectra (Dyson et al., 1974; Phelps & Sagalyn, 1976; Kelley et al., 1982; Lay et al., 2018; De Michelis et al., 2021).

Using the definition (6) one can deduce the phase scintillation index from its correlation function (17) as

$$\sigma_S^2 = \rho_S(0, s). \tag{20}$$

For the weak scattering regime, covered by the thin phase screen model, the intensity scintillation index (5) is expressed in terms of the log-amplitude correlation index as (Clifford & Yura, 1974; Fante, 1975a):

$$S_4^2 = \exp\left[4\rho_\chi(0, s)\right] - 1. \tag{21}$$

If $\rho_\chi(0, s) \ll 1$ it follows that $S_4^2 \approx 4\rho_\chi(0, s)$, cf. Ref. (Tatarski, 2016), that is a manifestation of log-normal statistics for the wave intensity under the quite ionospheric conditions.

4 Anisotropy of Ionospheric Irregularities

The scintillation-causing ionospheric irregularities show anisotropy and are mainly elongated in the direction of the geomagnetic lines of force (Tereshchenko et al., 1999; Portillo et al., 2008; Mevius et al., 2016; Liu et al., 2021). In order to include this anisotropy in the scintillation theory we assume that the surface of constant correlation of electron density fluctuations can be approximated by the concentric ellipsoidal shapes (Singleton, 1970; Moorcroft & Arima, 1972; Kersley et al., 1988; Bhattacharyya et al., 1992). For

[2] In order to underline the difference in scattering geometries considered within the spherical- (this article) and flat-geometry (Rino & Fremouw, 1977) approximations, we discuss the corresponding derivations of relationships between $\Phi_{\delta\varphi}$ and $\Phi_{\delta N_e}$ in Appendix D providing some further details.

the specified radius of correlation, r_0, the equation of ellipsoidal surface of constant correlation can be written as

$$\left(\frac{\Delta \mathtt{t}}{r_0}\right)^2 + \left(\frac{\Delta \mathtt{s}}{\alpha r_0}\right)^2 + \left(\frac{\Delta \mathtt{r}}{\beta r_0}\right)^2 = \text{const.} \tag{22}$$

Here $\Delta\mathtt{t}, \Delta\mathtt{s}, \Delta\mathtt{r}$ are the components of the position difference vector with respect to the so-called Singleton coordinate system $\mathtt{r}, \mathtt{s}, \mathtt{t}$. The latter is defined such that the coordinate center coincides with the center of the correlation ellipsoid and its coordinate axes are aligned along the major semi-axes of the ellipsoid. The $\mathtt{t}$-axis is chosen to be aligned along the minor semi-axis of length r_0 and the $\mathtt{s}$-axis is aligned along the major semi-axis of length αr_0. The remaining $\mathtt{r}$-axis is aligned along the semi-axis of length βr_0. The parameters α, β are the scaling factors characterizing the anisotropy of a particular ionospheric irregularity.

The correlation function of electron density fluctuations, $\rho_{\delta N_e}$, is assumed to depend on the quadratic form defined by Eq. (22). Similarly, the corresponding power spectral density, $\Phi_{\delta N_e}$, is the function of the similar diagonal quadratics in the reciprocal space $\kappa_\mathtt{r}, \kappa_\mathtt{s}, \kappa_\mathtt{t}$

$$Q(\kappa_\mathtt{t}, \kappa_\mathtt{s}, \kappa_\mathtt{r}) = r_0^2\kappa_\mathtt{t}^2 + (\alpha r_0)^2\kappa_\mathtt{s}^2 + (\beta r_0)^2\kappa_\mathtt{r}^2. \tag{23}$$

On the other hand, the expressions for the correlation and spectral density functions in Sec. 3 have been obtained as the function of coordinates $\boldsymbol{r}$ and $\boldsymbol{\kappa}$ associated with the wave propagation geometry, e.g., the z-axis has been chosen to be aligned with the wave vector $\boldsymbol{k}$ of the propagating radio wave. In order to incorporate the anisotropy effects, we thus need to perform a series of transformations of ellipsoid defined in the Singleton coordinates in order to redefine it in terms of the position difference variable components chosen in the conventional coordinate system x, y, z.

In order to perform the required coordinate transformation we follow the procedure given in Refs. (Rino & Fremouw, 1977; Rino, 1979a). For definiteness we consider the transformation in the spatial domain, i.e., for the moment we focus our attention on rotations of the correlation ellipsoid. For that we express Eq. (22) in terms of the conventional coordinate system, i.e., in terms of the position difference components $\Delta x, \Delta y, \Delta z$. This procedure involves the transformation from the conventional coordinates associated with the propagation geometry to the local coordinate system, e.g., the North-East-Down (NED) coordinate system with the origin at the center of the correlation ellipsoid and the consequent transformation from the NED coordinates to the Singleton ones. The last step is called the Singleton transformation and can be written using the notation n, e, d for the NED coordinates as

$$\begin{pmatrix} \Delta\mathtt{s} \\ \Delta\mathtt{r} \\ \Delta\mathtt{t} \end{pmatrix} = R_x(\gamma)R_y(\psi)R_z(\delta) \begin{pmatrix} \Delta n \\ \Delta e \\ \Delta d \end{pmatrix}, \tag{24}$$

where δ is the magnetic dip angle, ψ is the magnetic declination angle, and γ is the tilt angle of the magnetic field lines. The rotation matrices

$$R_x(\xi) = \begin{pmatrix} 1 & 0 & 0 \\ 0 & \cos\xi & -\sin\xi \\ 0 & \sin\xi & \cos\xi \end{pmatrix}, \quad R_y(\xi) = \begin{pmatrix} \cos\xi & 0 & \sin\xi \\ 0 & 1 & 0 \\ -\sin\xi & 0 & \cos\xi \end{pmatrix},$$
$$R_z(\xi) = \begin{pmatrix} \cos\xi & -\sin\xi & 0 \\ \sin\xi & \cos\xi & 0 \\ 0 & 0 & 1 \end{pmatrix}$$

perform the rotations on angle ξ with respect to the corresponding x, y or z axis. The geometrical meaning of rotational transformations in Eq. (24) can be inferred from Fig. 1.

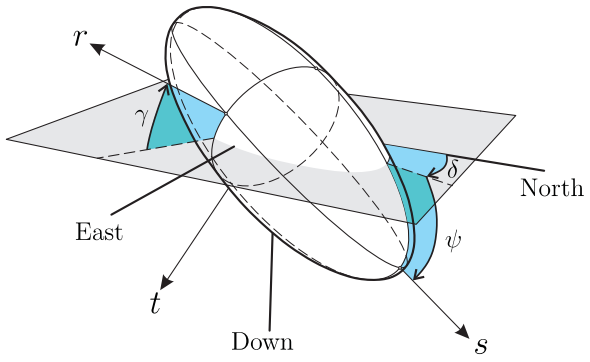

Figure 1. Orientation of the ellipsoid of constant correlation in the North-East-Down (NED) local coordinate system. The principal axes of the ellipsoid are aligned along the Singleton coordinate axes $\mathtt{s}, \mathtt{r}, \mathtt{t}$ and are rotated with respect to the NED coordinates on the magnetic declination, δ, magnetic inclination (dip), ψ, and tilt, γ, angles.

The transformation of the components of the position difference vector defined in the conventional coordinates to the components in the NED-coordinate system is

$$\begin{pmatrix} \Delta n \\ \Delta e \\ \Delta d \end{pmatrix} = R_z(-\phi_p) R_y(\theta_p) \begin{pmatrix} \Delta x \\ \Delta y \\ \Delta z \end{pmatrix}, \tag{25}$$

where ϕ_p and θ_p are the azimuth and nadir (zenith) angles of the wave propagation path at the location of the ionospheric scattering point, see also Fig. 2. The relationships between the local coordinates ϕ_p, θ_p and the coordinates of the sender and the receiver are summarized in Appendix A. The combination of Eqs. (24) and (25) yields the required transformation from the conventional coordinates x, y, z to the Singleton coordinates $\mathtt{r}, \mathtt{s}, \mathtt{t}$.

The diagonal quadratic form (22) is expressed in terms of the NED coordinates as

$$\begin{aligned} q(\Delta n, \Delta e, \Delta d) &= \begin{pmatrix} \Delta n & \Delta e & \Delta d \end{pmatrix} \cdot C \begin{pmatrix} \Delta n \\ \Delta e \\ \Delta d \end{pmatrix}, \\ C &= \left[D^{-1} R_x(\gamma) R_y(\psi) R_z(\delta) \right]^T D^{-1} R_x(\gamma) R_y(\psi) R_z(\delta). \end{aligned} \tag{26}$$

Here

$$D = r_0 \begin{pmatrix} \alpha & 0 & 0 \\ 0 & \beta & 0 \\ 0 & 0 & 1 \end{pmatrix} \tag{27}$$

is the scaling matrix that deforms isotropic correlation surface, i.e., the sphere of unit radius, into the required ellipsoidal surface. The elements of the matrix C are calculated as

$$\begin{aligned} C_{11} &= \frac{1}{r_0^2} \left[\alpha^{-2} \cos^2\psi \cos^2\delta + \sin^2\psi \cos^2\delta \left(\cos^2\gamma + \beta^{-2} \sin^2\gamma \right) \right. \\ &+ \left. \sin^2\delta \left(\sin^2\gamma + \beta^{-2} \cos^2\gamma \right) + \frac{1}{2} \sin 2\gamma \sin\psi \sin 2\delta \left(\beta^{-2} - 1 \right) \right], \\ C_{22} &= \frac{1}{r_0^2} \left[\alpha^{-2} \cos^2\psi \sin^2\delta + \sin^2\psi \sin^2\delta \left(\cos^2\gamma + \beta^{-2} \sin^2\gamma \right) \right. \\ &+ \left. \cos^2\delta \left(\sin^2\gamma + \beta^{-2} \cos^2\gamma \right) - \frac{1}{2} \sin 2\gamma \sin\psi \sin 2\delta \left(\beta^{-2} - 1 \right) \right], \\ C_{33} &= \frac{1}{r_0^2} \left[\alpha^{-2} \sin^2\psi + \cos^2\psi \left(\cos^2\gamma + \beta^{-2} \sin^2\gamma \right) \right], \end{aligned} \tag{28}$$

261

$$
\begin{aligned}
C_{12} &= C_{21} = \frac{1}{2r_0^2}\sin 2\delta\left[\sin^2\gamma + \beta^{-2}\cos^2\gamma - \alpha^{-2}\cos^2\psi - \sin^2\psi\left(\cos^2\gamma + \beta^{-2}\sin^2\gamma\right)\right] \\
&+ \frac{r_0^2}{2}\cos 2\delta \sin 2\gamma \sin\psi\left(\beta^{-2}-1\right), \\
C_{13} &= C_{31} = \frac{1}{2r_0^2}\sin 2\psi\cos\delta\left(\alpha^{-2} - \cos^2\gamma - \beta^{-2}\sin^2\gamma\right) - \frac{1}{2r_0^2}\sin 2\gamma\cos\psi\sin\delta\left(\beta^{-2}-1\right), \\
C_{23} &= C_{32} = -\frac{1}{2r_0^2}\sin 2\psi\sin\delta\left(\alpha^{-2} - \cos^2\gamma - \beta^{-2}\sin^2\gamma\right) - \frac{1}{2r_0^2}\sin 2\gamma\cos\psi\cos\delta\left(\beta^{-2}-1\right).
\end{aligned}
$$

262 The particular case of $\delta = 0$ has been considered in Ref. (Rino & Fremouw, 1977).

In order to express the quadratic form (22) in terms of the x, y, z coordinates, one need to perform the final transformation according to Eq. (25). For the sake of convenience we switch to the similar quadratic form (23) defined in the reciprocal space. It can be expressed in terms of the spatial frequency vector $\boldsymbol{\kappa}$, reciprocal to the argument $\boldsymbol{r}_1 - \boldsymbol{r}_2 = (\Delta x \quad \Delta y \quad \Delta z)^T$ of the autocorrelation function (14), as

$$
Q(\boldsymbol{\kappa}) = \Big[R_z(-\phi_p)R_y(\theta_p)\boldsymbol{\kappa}\Big]^T \cdot \overline{C}\, R_z(-\phi_p)R_y(\theta_p)\boldsymbol{\kappa}, \tag{29}
$$

where the matrix $\overline{C}$ is obtained from the matrix C, by performing the replacement: $r_0 \to 1/r_0$, $\alpha \to 1/\alpha$, $\beta \to 1/\beta$ in Eq. (28). The calculation of the quadratic form (29) can be simplified by noting that the calculation of scintillation indices requires the knowledge of the quadratic form $Q(\boldsymbol{\kappa}_\perp, 0)$, where the spatial vector component along the propagation direction is set to zero, see Eq. (18). This simplification yields

$$
Q(\boldsymbol{\kappa}_\perp, 0) = \mathcal{A}\kappa_x^2 + 2\mathcal{B}\kappa_x\kappa_y + \mathcal{C}\kappa_y^2, \tag{30}
$$

263 where

$$
\begin{aligned}
\mathcal{A} &= \overline{C}_{11}\cos^2\theta_p\cos^2\phi_p + \overline{C}_{22}\cos^2\theta_p\sin^2\phi_p + \overline{C}_{33}\sin^2\theta_p \\
&- \overline{C}_{12}\cos^2\theta_p\sin 2\phi_p - \overline{C}_{13}\sin 2\theta_p\cos\phi_p + \overline{C}_{23}\sin 2\theta_p\sin\phi_p, \qquad (31) \\
\mathcal{B} &= \frac{1}{2}\left(\overline{C}_{11} - \overline{C}_{22}\right)\cos\theta_p\sin 2\phi_p + \overline{C}_{12}\cos\theta_p\cos 2\phi_p - \overline{C}_{13}\sin\theta_p\sin\phi_p - \overline{C}_{23}\sin\theta_p\cos\phi_p, \\
\mathcal{C} &= \overline{C}_{11}\sin^2\phi_p + \overline{C}_{22}\cos^2\phi_p + \overline{C}_{12}\sin 2\phi_p.
\end{aligned}
$$

264 The quadratic form (30) corresponds to the elliptical cross-section of the ellipsoid (23)
265 with the plane of the phase screen.

273 Incorporating formula (30) in the von Karman spectrum (19) one obtains for the
274 properly normalized spectrum the following expression:

$$
\Phi_{\delta N_e}(\boldsymbol{\kappa}_\perp, 0) = \alpha\beta r_0^3 C_s \frac{r_0^{p-1}}{\left(\mathcal{A}\kappa_x^2 + 2\mathcal{B}\kappa_x\kappa_y + \mathcal{C}\kappa_y^2 + r_0^2\kappa_0^2\right)^{\frac{p+2}{2}}}. \tag{32}
$$

Here

$$
C_s = \frac{\langle \delta N_e^2 \rangle}{\pi^{\frac{3}{2}}} \frac{\Gamma\left(\frac{p+2}{2}\right)}{\Gamma\left(\frac{p-1}{2}\right)} \kappa_0^{p-1} \tag{33}
$$

275 is the so-called structure parameter. This particular type of spectrum would be used in
276 the following

277 5 Anisotropic Scintillation Indices

278 In this section we will use the spectral model (32) for calculations of the anisotropic
279 scintillation indices. To this end one can substitute the power spectral density of the elec-
280 tron density fluctuations (32) in Eq. (18). The latter equation is then used in Eqs. (16)

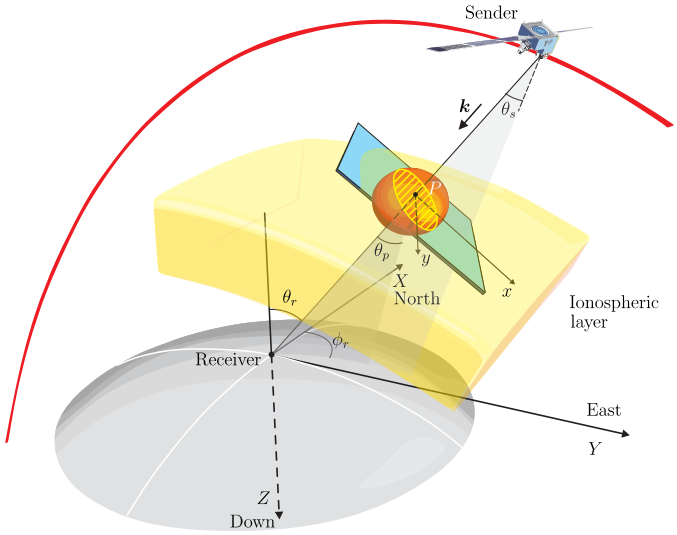

Figure 2. Scattering geometry for the signal that propagates in the disturbed ionosphere. The relative position of the sender, receiver and the scattering point P defines the plane of the phase screen which is transversal to the wave vector of the signal wave. This plane crosses the correlation ellipsoid and forms the elliptic cross-section (hatched area). Some used coordinate systems are indicated along with the zenith (nadir) angles θ_r, θ_p, θ_s and the receiver azimuth angle ϕ_r.

and (17) for calculation of the log-amplitude and phase correlation functions. The resulting integrals can be simplified by making certain observations as discussed below.

If one defines the spatial frequency associated with the radius of the first Fresnel zone as $\kappa_f = 2\pi/\sqrt{\lambda s}$ it is reasonable to consider the following spatial frequency ranges: $\kappa_\perp < \kappa_f$ and $\kappa_\perp > \kappa_f$. A particular spatial frequency $\kappa_\perp$ is inversely proportional to the scale of the associated irregularity if this scale is measured along the direction perpendicular to the propagation direction. In the first case of $\kappa_\perp < \kappa_f$, the inhomogeneities are large enough to bend the propagating signal ray. Such refraction scintillation primarily contributes to the random excursion of the phase (Conroy et al., 2022). The amplitude scintillation is negligibly small as the propagation factor $\sin^2(s\kappa_\perp^2/2k)$ found in the integral (16) tends to zero. For the phase fluctuations the corresponding propagation factor $\cos^2(s\kappa_\perp^2/2k)\approx 1$ and the phase scintillation index is primarily associated with the refractive effects. The latter can be written by combining Eqs. (32), (18), (17) and (20) as

$$\sigma_S^2 \approx 2\pi\alpha\beta\,\lambda^2 r_e^2 C_s\,\Delta s\, r_0^3 \int\limits_{\mathbb{R}^2} \frac{r_0^{p-1}\mathrm{d}^2\boldsymbol{\kappa}_\perp}{\left(\mathcal{A}\kappa_x^2 + 2\mathcal{B}\kappa_x\kappa_y + \mathcal{C}\kappa_y^2 + r_0^2\kappa_0^2\right)^{\frac{p+2}{2}}} \tag{34}$$

This type of phase fluctuations has been treated in (Rino, 1979a).

In the second case of $\kappa_\perp > \kappa_f$, the propagation factor in Eq. (16) is finite and shows the oscillating behavior. We can however make the reasonable approximation $\kappa_0 \ll \kappa_f$, i.e., we assume that the transversal scales of the scintillation associated irregularities are smaller than the largest spatial scale of ionospheric inhomogeneities. Such small-scale irregularities contribute merely to the random diffraction of the transmitted electromagnetic waves giving rise primarily to the amplitude scintillation. Additionally to this the major contribution is due to the irregularity scales corresponding to the radius of the first Fresnel zone $\sqrt{\lambda s}$. The log-amplitude scintillation index can be approximated then

as

$$S_4^2 \approx \exp\left[8\pi\alpha\beta\,\lambda^2 r_e^2 C_s\,\Delta s\,r_0^3 \int\limits_{\mathbb{R}^2} \frac{r_0^{p-1}\sin^2\left(\frac{s\kappa_\perp^2}{2k}\right)}{\left(\mathcal{A}\kappa_x^2 + 2\mathcal{B}\kappa_x\kappa_y + \mathcal{C}\kappa_y^2\right)^{\frac{p+2}{2}}}\mathrm{d}^2\boldsymbol{\kappa}_\perp\right] - 1. \tag{35}$$

Here we have used the condition $\kappa_0 \ll \kappa_f \leq 2\pi/r_0$ along with $r_0\kappa_0 \to 0$ while the value of the outer scale wave number remains finite.

The calculation of integrals in Eqs. (34) and (35) is outlined in Appendix E. The resulting scintillation indices then read as

$$\sigma_S^2 \approx 4\pi^2 C_s \mathcal{G}\,p^{-1}\,\Delta s\,\lambda^2 r_e^2 \kappa_0^{-p} \tag{36}$$

$$\begin{aligned} S_4^2 \quad \approx \exp\Bigg[&8\pi^{\frac{5}{2}} C_s\,\mathcal{G}\,\frac{1}{p}\frac{\Gamma\left(1-\frac{p}{4}\right)}{\Gamma\left(\frac{1}{2}+\frac{p}{4}\right)}\,\Delta s\,\lambda^2 r_e^2\left(\frac{s\,r_0^2}{2k}\right)^{\frac{p}{2}} \\ &\times\left(\frac{1}{\sqrt{\mathcal{A}\mathcal{C}-\mathcal{B}^2}}\right)^{\frac{p}{2}} P_{\frac{p}{2}}\left(\frac{\mathcal{A}+\mathcal{C}}{2\sqrt{\mathcal{A}\mathcal{C}-\mathcal{B}^2}}\right)\Bigg] - 1, \end{aligned} \tag{37}$$

where

$$\mathcal{G} = \frac{\alpha\beta r_0^2}{\sqrt{\mathcal{A}\mathcal{C}-\mathcal{B}^2}} \tag{38}$$

is the so-called geometric factor and $P_\alpha(x)$ is the Legendre function of order α.

The reference (Rino, 1979a) gives[3] the following interpretation of the result (37). The scintillation index S_4^2 is proportional to $C_s\,\kappa_f^{-p}$, where $\kappa_f = 2\pi/\sqrt{\lambda s}$ is the Fresnel spatial frequency. Comparing this power law dependence with the three-dimensional spectrum for electron density fluctuations (19), one can conclude that the magnitude of S_4 is modulated by the one-dimensional power spectral density of ionospheric irregularities evaluated at the spatial frequency associated with the radius of the first Fresnel zone for the considered scattering geometry. We also note that both expressions for scintillation indices do not depend on the correlation radius r_0 as one would expect.

The obtained expressions (36) and (37) can be compared with the seminal results of (Rino, 1979a) which can be written in the following form:

$$\sigma_{S,\mathrm{Rino}}^2 \approx 4\pi^2 C_s \mathcal{G}'\,p^{-1}\,\Delta h\,\sec\theta\,\lambda^2 r_e^2 \kappa_0^{-p} \tag{39}$$

$$\begin{aligned} S_{4,\mathrm{Rino}}^2 \quad \approx \exp\Bigg[&8\pi^{\frac{5}{2}} C_s\,\mathcal{G}'\,\frac{1}{p}\frac{\Gamma\left(1-\frac{p}{4}\right)}{\Gamma\left(\frac{1}{2}+\frac{p}{4}\right)}\,\Delta h\sec\theta\,\lambda^2 r_e^2\left(\frac{h_p\sec\theta\,r_0^2}{2k}\right)^{\frac{p}{2}} \\ &\times\left(\frac{1}{\sqrt{\mathcal{A}'\mathcal{C}'-(\mathcal{B}')^2}}\right)^{\frac{p}{2}} P_{\frac{p}{2}}\left(\sec\theta\frac{\mathcal{A}'+\mathcal{C}'-\mathcal{A}'a_1^2-2\mathcal{B}'a_1a_2-\mathcal{C}'a_2^2}{2\sqrt{\mathcal{A}'\mathcal{C}'-(\mathcal{B}')^2}}\right)\Bigg] - 1, \end{aligned} \tag{40}$$

where we extended the applicability of the single scattering result for S_4 index according to Eq. (21). Here the geometric term is defined as

$$\mathcal{G}' = \frac{\alpha\beta\,r_0^2\sec\theta}{\sqrt{\mathcal{A}'\mathcal{C}'-(\mathcal{B}')^2}}, \tag{41}$$

[3] Note that the spectral index of Ref. (Rino, 1979a), ν, is related to the one-dimensional spectral index of electron density fluctuations, p, as $\nu = (p+1)/2$.

where the quadratic form coefficients are

$$\begin{aligned}\mathcal{A}' &= \overline{C}_{11} + \overline{C}_{33}\tan^2\theta\cos^2\phi - 2\overline{C}_{13}\tan\theta\cos\phi,\\ \mathcal{B}' &= \overline{C}_{12} + \frac{1}{2}\overline{C}_{33}\tan^2\theta\sin 2\phi - \tan\theta\Big(\overline{C}_{13}\sin\phi + \overline{C}_{23}\cos\phi\Big),\\ \mathcal{C}' &= \overline{C}_{22} + \overline{C}_{33}\tan^2\theta\sin^2\phi - 2\overline{C}_{23}\tan\theta\sin\phi.\end{aligned} \tag{42}$$

These coefficients have an another functional dependence as the coefficients in Eq. (31) as a consequence of the flat-geometry approximation used in Rino's theory and the difference in how the phase screen plane is positioned in space. Namely Rino's theory defines the phase screen plane to be transversal to the vertical direction of the ground observer, while in the spherical-geometry approximation, developed in this article, it is transversal to the wave vector of the propagating signal wave.

Another consequence of the flat-geometry approximation is the equivalence of zenith (nadir) and azimuth angles for the sender, the receiver, and the scattering point. Because of this equivalence we have omitted corresponding indices in Eqs. (39) - (42) for the zenith, θ, and the azimuth, ϕ, angles.

We also note that the positioning of the phase screen plane to be perpendicular to the observer vertical direction is optimal for the description of the signal propagation when the sender is at the receiver zenith. For the slant sender-receiver links the correction term $\mathcal{A}'a_1^2 + 2\mathcal{B}'a_1a_2 + \mathcal{C}'a_2^2$ appears in the argument of the Legendre function in Eq. (40). The arguments of this quadratic form, $a_1 = \sin\theta\cos\phi$, $a_2 = \sin\theta\sin\phi$, are the projections of the normalized wave vector $\boldsymbol{k}/k$ on the phase screen plane.

6 Geometric enhancement of scintillation

The scintillation indices (36) and (37) [as well as the indices (39) and (40)] depend on the set of parameters that can be deduced from the experimental data. The integrated irregularity strength parameter $C_s\Delta h$ can be retrieved from the GNSS and SAR satellite scintillation measurements (Belcher et al., 2017; Mohanty et al., 2018; Carrano et al., 2019; Helmboldt & Zabotin, 2022; Ji et al., 2022)[4]. This parameter exhibits dependence on the season, time, magnetic latitude, solar activity, etc. Based on the empirical data, the climatological model $C_s\Delta h$ has been developed within the framework of the WBMOD (Fremouw & Larsinger, 1981; Secan & Fremouw, 1983; Fremouw & Secan, 1984; Secan et al., 1987).

The value of the spectral index p depends on the type of instability involved in the formation of ionospheric irregularities responsible for the random scattering of the signal wave. The typical empirical and theoretical values of p are summarized in Ref. (Vasylyev et al., 2022).

The anisotropy parameters α and β have a rich morphology. At high latitudes one has observed the rod-like structures ($\alpha \approx 5-10, \beta \approx 1$) that are elongated along the geomagnetic field lines (Rino et al., 1978; Sunanda Basu et al., 1991; Wang & Morton, 2017; Conroy et al., 2021). Additionally to these structures, the wing- ($\alpha \approx 10{-}15, \beta \approx 5$) and sheet-like ($\alpha \approx \beta \approx 10$) structures might appear near the exit of the polar convection channel (Rino & Owen, 1980; Rino et al., 1983; Conroy et al., 2021). The mid-latitude irregularities are primarily field-aligned of the rod-type, $\alpha \approx 6, \beta \approx 1$, (Moorcroft & Arima, 1972) (Lay et al., 2018), while the Perkin instability might also form the sheet-like structures (MacDougall & Eadie, 2005). Finally, the equatorial irregularities show a high degree of anisotropy. For example, ellipse-like diffraction patterns on the ground

[4] The relationship of the parameter $C_s\Delta h$, with C_s as defined in Eq. (33), to the parameter C_kL of, e.g., Ref. (Carrano et al., 2019) is $C_s\Delta h = \frac{1}{(2\pi)^3}\left(\frac{2\pi}{1000}\right)^{p+2}\cdot C_kL$.

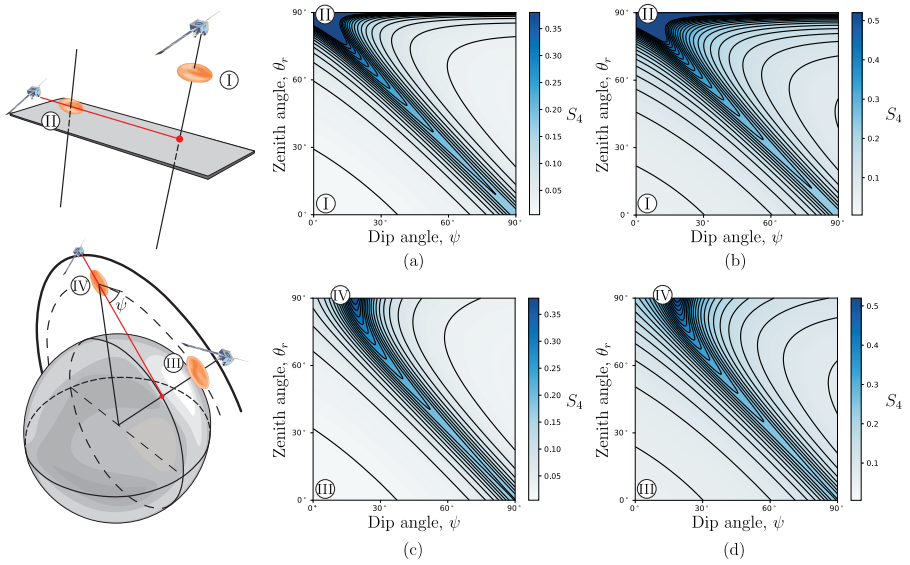

Figure 3. Enhancement of the amplitude scintillation calculated within the flat-geometry, (a) and (b), and the spherical-geometry, (c) and (d), approximations. Two types of irregularities have been considered in the calculations: wing-like structures with α=10, β=5, figures (a) and (c); rod-like inhomogeneities with α=10 and β=1, figures (b) and (d). The Roman numbers indicate regions of values for the receiver zenith angle, θ_r, and for the geomagnetic dip angle, ψ, that correspond to the propagation link configurations sketched on the first column of the figure. The receiver azimuth, magnetic declination, and tilt angles are set to be zero.

formed by these irregularities show their elongation along the magnetic field lines and the axial ratio to reach the value of 60:1 (Koster, 1963, 1972).

In order to demonstrate the impact of these anisotropy factors along with the type of approximation for the link configuration on the geometric enhancement of scintillation, we plot in Fig. 3 the amplitude scintillation index as a function of the receiver zenith angle and the geomagnetic dip angle. The scintillation index is shown for two types of ionospheric irregularities: wing-like ones, plots (a), (c), and the rod-like structures, plots (b), (d). Despite the plots for both types of irregularities look similar, one can observe that in the case when the irregularity is primarily elongated along only one direction (rod-like structure) the enhancement of scintillation is stronger, plots (b), (d), than in the case when the irregularities are highly anisotropic, as it is the case for the wing-like structures, plots (a) and (c).

The upper row of the plots, Figs. 3 (a), (b), corresponds to the flat-geometry approximation and Eq. (40) is used for the calculation of S_4. Correspondingly, the plots (c), (d) from the lower row of Fig. 3 represent the spherical-geometry approximation, cf. Eq. (37). The graphics in the first column of Fig. 3 sketches the geometry of the sender-receiver links crossing the ionospheric irregularities at two limiting values of the receiver zenith angle, namely, for θ_r=0° as indicated by the Roman numbers I, III and for θ_r=90° as indicated by II and IV. The shown ellipsoids correspond to the isosurfaces of the constant correlation, cf. Eq. (22). Using these sketches as a visual aid one can interpret the difference in geometric enhancement regions shown in Figs. 3 (a), (b) and in Figs. 3 (c), (d) as follows.

For the vertical propagation links, marked by I and III, the scintillation index attains small values at small magnetic dip angles. In this case the link crosses the corre-

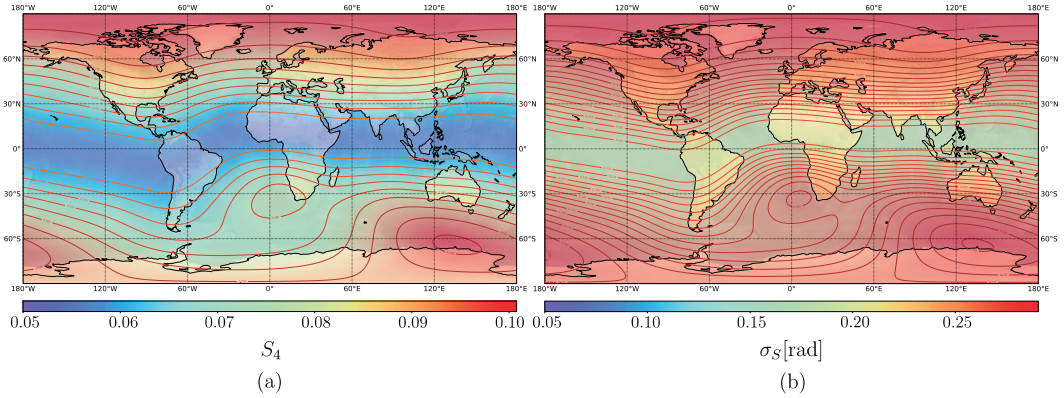

Figure 4. Amplitude, (a), and phase, (b), scintillation indices calibrated by the condition $C_s\Delta h$=const. The indices are calculated for the zenith angle θ_p=θ_r=0 and the azimuth angle ϕ_p=θ_r=0. The height of the scattering point is taken to be equal to the ionospheric piercing point (350 km). The anisotropy parameters are set to α=2, $\beta = 1.5$.

lation ellipsoid along one of its minor semi-axis. The dimension of a typical irregularity along this crossing line is small and the resulting random phase increment is also small, cf. Eq. (8). If we change the zenith angle to θ_r=90°, that corresponds to the cases II and IV, the small values of the dip angle would correspond to the situation when the link crosses the correlation ellipsoids along the major semi-axis. In this case the length of propagation path in random medium is larger, the disruptive effects of the propagating signal are stronger, and the resulting scintillation both in amplitude and phase are enhanced. One can also note the divergent character of indices obtained within the flat-geometry approximation at θ_r=90°. This is because the scintillation indices (39) and (40) depend on the mapping function $\sec\theta_r$, which diverges as $\theta_r \to 90°$.

One also notes the difference in the position of the regions of enhanced S_4 for the flat- and spherical geometry approximations at large zenith angles. For the flat-geometry approximation the maximal value of the enhancement is obtained for the dip angle ψ=0°. In the case of the spherical-geometry approximation the region of enhanced scintillation shifts to finite values of the dip angle. This happens because the correlation ellipsoid should be inclined to the local horizontal plane at the scattering point in order that the propagation path, horizontal for the receiver, would cross the ellipsoid along the major semi-axis. This is purely geometric effect related to the finiteness of the radii of curvature of the Earth surface and of the ionospheric shell.

In Fig. 3 and in the following figures we have set the irregularity strength parameter to be the constant with the value $C_s\Delta h = 4.77\times10^{22}\mathrm{m}^{-p-4}$ with p being the spectral index. By doing so we neglect any effects connected with the morphology of $C_s\Delta h$ and thus the calculated scintillation indices represent not the true scintillation levels but the geometric enhancement contributions to these levels. We also note that the chosen value for $C_s\Delta h$ corresponds to $C_k\,L = 10^{33}\mathrm{m}^{-p-4}$ of the WBMOD model, which is approximately the value observed at the magnetic equator (Rogers et al., 2014; Mohanty et al., 2018).

Figures 4–6 show the regions of enhanced scintillation for several link configurations on the global scale. The values for the magnetic declination, δ, and dip, ψ, angles are obtained from the International Geomagnetic Reference Field (IGRF) model of the 13^{th} generation (Alken et al., 2021). The tilt angle γ is set to zero.

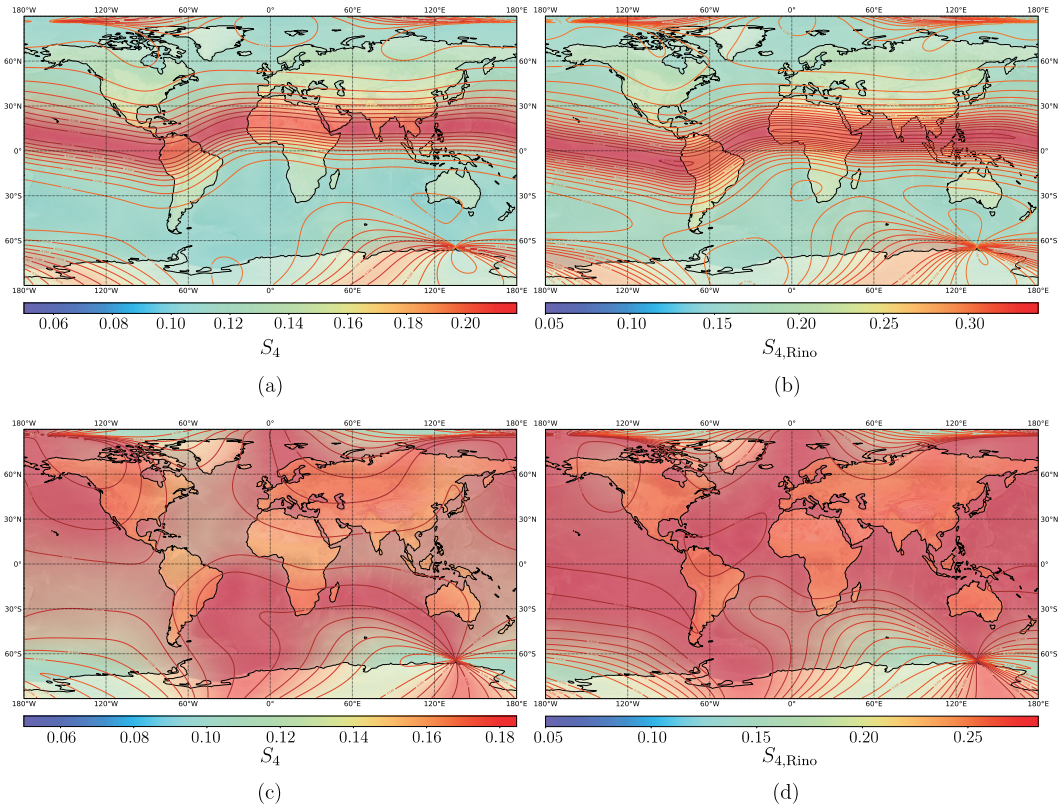

Figure 5. Amplitude scintillation indices in the spherical-, plots (a) and (c), and in the flat-geometry approximations, plots (b) and (d). The receiver zenith angle is θ_r=85° that corresponds to the zenith angle at scattering point on plots (a) and (c) $\theta_p = 40.9°$. The azimuth angles at the scattering point are: $\phi_p = 0°$ for plots (a) and (b); $\phi_p = 90°$ for plots (c) and (d). Other parameters are the same as for Fig. 4.

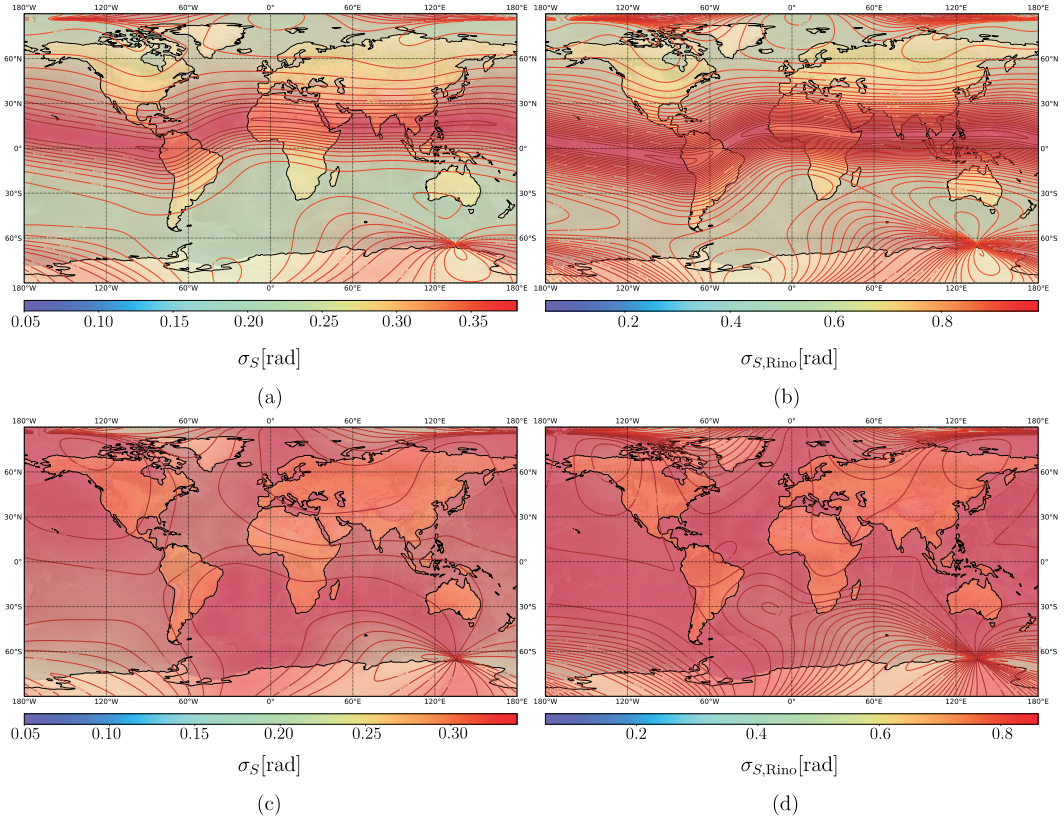

Figure 6. Phase scintillation maps shown for the same parameters as used in Fig. 5.

For the vertical propagation path, cf. Fig. 4, both amplitude and phase scintillation indices exhibit the geometric enhancement merely at polar regions. At poles the anisotropic ionospheric irregularities lie within L shells and are elongated along almost vertical direction to the ground-based observer. The signal wave is thus the worst affected by scintillation while propagating along the vertical direction. The effect of the geometric enhancement in the polar regions for the near vertical links has been previously discussed in (Forte & Radicella, 2004).

In another extreme case when the sender-receiver link is nearly horizontal, cf. Figs. 5 and 6, the behavior of regions of enhanced scintillation depends strongly on the receiver azimuth angle. For the azimuth angle ϕ_r=0° this region shifts from the northern pole towards the magnetic equator, where the orientation of field-aligned irregularities is given by small values of the geomagnetic dip angle. The exact position of this enhancement belt depends on the receiver azimuth angle on the geometric approximation that is used. For example, by comparing Figs. 5 (a) and (b) one observes that the flat-geometry approximation, case (b), yields the enhancement belt that is shifted more towards the magnetic equator in comparison to the spherical geometry approximation result, cf. plot (a). This shift of the enhancement belt for different approximation is again connected with the difference in values of the dip angle at the receiver horizon, cf. for example Fig. 3, cases II and IV.

If the receiver azimuth angle is changed to ϕ_r=90° the map of the geometric enhancement of scintillation exhibits a more uniform distribution of values with some reduced scintillation levels near the magnetic poles, cf. Figs. 5 (c), (d) and 6 (c), (d). This uniformity is connected with the geometry of sender-receiver links that cross the corre-

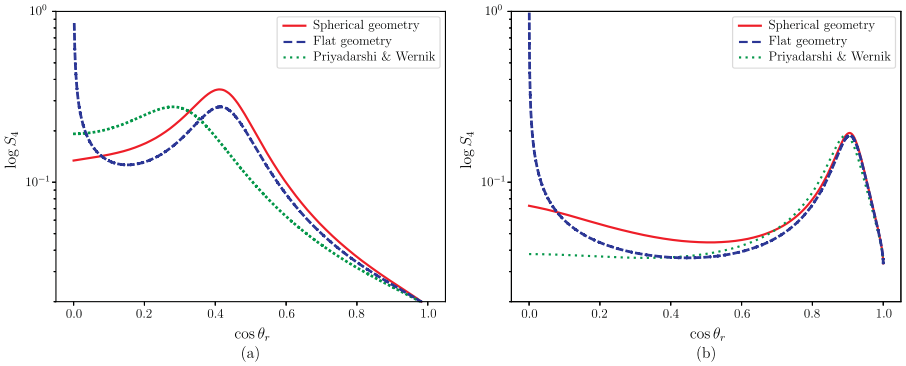

Figure 7. Amplitude scintillation index as a function of the receiver zenith angle calculated using the spherical-geometry approximation, the flat-geometry approximation (Rino, 1979a), and the Priyadarshi and Wernik correction to the flat-geometry approximation (Priyadarshi & Wernik, 2013) for the dip angle ψ=25° (a) and ψ=65° (b). The parameters used in the calculation are: the spectral index p=1.6, the anisotropy parameters α=10 and β=5, the magnetic declination, δ, and the tilt, γ, angles are set to zero.

lation ellipsoids in the directions near or along of one of the minor semi-axes. By comparing Fig. 5 (c) with Fig. 5 (d) or the corresponding plots in Fig. 6 one can note that the regions of enhancement are almost complimentary to each other if calculated using different geometrical models. This observation shows that the accounting for the finiteness of the Earth surface curvature becomes essential for very slant propagation links and the use of the flat-geometry approximation might mislead in estimation of regions of geometrically enhanced scintillation. One can also note that the flat-geometry approximation, cf. Fig. 5 (b), (d) and 6 (b), (d), yields higher values of the scintillation index for almost horizontal links in comparison to the spherical-geometry approximation, cf. Fig. 5 (a), (c) and 6 (a), (c).

We now compare the amplitude scintillation index calculated by using the proposed spherical-geometry approximation, the flat-geometry approximation of (Rino, 1979a), and the corrected flat-geometry approximation (Priyadarshi & Wernik, 2013). The latter correction is based on Eqs. (39) and (40) where the zenith angle is adjusted in order to account for the finiteness of the earth curvature according to

$$\theta = \arccos\left(\sqrt{1 - \left(\frac{R_\oplus + h_r}{R_\oplus + h_p}\sin\theta_r\right)^2}\right), \tag{43}$$

where $R_\oplus$ is the Earth radius, h_p and h_r are the altitudes of the phase screen and of the receiver, respectively. Figure 7 demonstrates the comparison of these models for the case of the wing-like irregular structures. One can see that both flat- and spherical-geometry approximations yield comparable results for almost all values of the zenith angle. The flat-geometry approximation shows however the divergent behaviour as $\theta_r \to 90°$. This is a consequence of the divergent nature of the secant as a function of the zenith angle for nearly horizontal propagation links. The corrected flat-geometry approximation according to Ref. (Priyadarshi & Wernik, 2013) do not show such a divergent character but the position of the peak of enhancement appears to be displaced in comparison to other two models. One can see that apart from the cases of nearly horizontal links all three formulations provide the comparable results.

To conclude the discussion of the geometric effect of scintillation we consider the radio communication links from a geostationary satellite over the equator broadcasting at the VHF. For this case the regions of enhanced scintillation are shown in Fig. 8. One

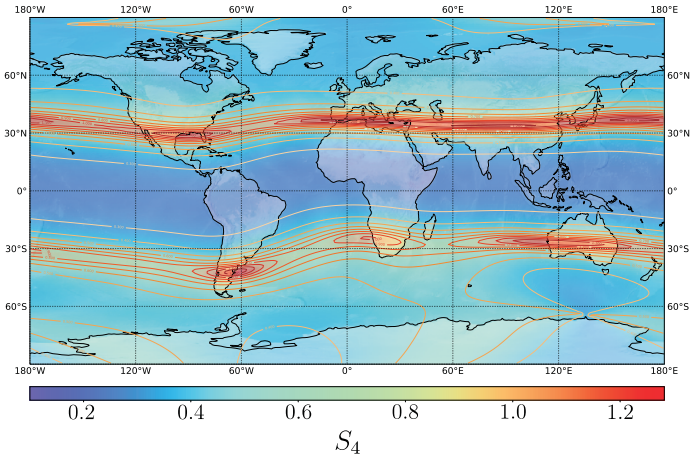

Figure 8. Geometric enhancement of scintillation for a VHF signal from a geostationary satellite over the equator. The value of $C_s\Delta h$ is set to be constant and corresponds to the typical value at the magnetic equator. The irregularity anisotropy parameters are α=10, β=2 and the spectral index p=1.6.

can see two bands of geometrically enhanced amplitude scintillation situated at mid-latitudes of both Earth hemispheres. Such type of the enhancement has been discussed previously in (Sinno & Minakoshi, 1983), where it has been discovered that scintillation in signals from the ETS-II geostationary satellite detected in Japan are more severe than has been expected. This enhancement has been explained via the geometric effect using the theoretical formulation of (Mikkelsen et al., 1978). The calculations based on Eq. (37) reproduce the regions of enhanced scintillation in a full agreement with Ref. (Sinno & Minakoshi, 1983). This can be seen when comparing Fig. 8 with analogous Fig. 5 of Ref. (Sinno & Minakoshi, 1983). The position of the bands of enhanced scintillations at mid-latitudes is related to the link specifics between the ground receiver at these latitudes and the satellite at the geostationary orbit. While calculating the enhancement levels in Fig. 8 we assumed that each communication link with the satellite lies within the receiver meridian and the receiver position has been scanned along the longitude and latitude ranges shown in the figure. Such particular links cross the anisotropic irregularities almost along the major semi-axis at mid-latitudes, and, hence, the scintillation of the transmitted VHF signals are geometrically enhanced.

7 Conclusions

Anisotropy is a remarkable feature of the ionospheric scintillation phenomena. The irregular ionospheric structures that distort propagating radio signals are usually field-aligned and elongated along the magnetic lines of force. Correspondingly, if the signal transverses such an irregularity along the elongation axis it propagates a longer path and experiences cumulatively larger distortions in comparison to the signal propagating along in some perpendicular direction. The level of the signal distortion in amplitude and phase, characterized by the corresponding scintillation indices, is thus highly dependent on the geometry of radio propagation path, the position of the ionospheric irregularity relative to this path, and on the anisotropy parameters.

Within the context of several important applications of radio communication or sensing channels, such as the GNSS navigation and positioning services, SAR imaging and interferometry, reflectometry, and occultation remote sensing techniques, the proper accounting of anisotropy in scintillation is of considerable importance. In some cases these

applications utilize the sender-receiver links with small elevation angles (large zenith angles). The popular approach for estimating the levels of anisotropic scintillation indices developed in Refs. (Rino & Fremouw, 1977; Rino, 1979a) uses the assumption that the communication or sensing links are nearly vertical with respect to the receiving station. This limitation is posed by the assumption that the curvature of the Earth surface and of the ionospheric shell can be neglected. The application of this formulation to the highly slant links yields non-physical artifacts such as the divergent behaviour of the scintillation indices.

In the present article we reconsidered the classical results of Ref. (Rino, 1979a) with the focus on the consistent geometric formulation of the problem and propose the spherical-geometry approximation. Within the framework of this approximation the Earth surface and the ionospheric layer have been assumed to exhibit spherical symmetry. This allowed us to remove the restriction on the signal propagation links to be nearly vertical. As a consequence, the derived scintillation indices do not exhibit the divergent behavior at small elevation angles. Moreover, due to the finiteness of curvatures of the ionospheric shell and of the Earth surface the regions of geometrically enhanced scintillation are displaced in parameter space when compared to the results of the flat-geometry approximation utilized in Ref. (Rino, 1979a). Two factors are responsible for this displacement. Firstly, the flat-geometry approximation contains no distinction of the local coordinates of the receiver and of the point along the signal propagation path where the incoming signal wave scatters on the ionospheric irregularity. In contrast to this, the zenith and azimuth angles of the receiver and of the scattering point differ from each other. As a consequence, the regions of enhanced scintillation are displaced in zenith and azimuth at small elevation angles for the realistic propagation links compared to those obtained under the flat-geometry approximation. Secondly, the finiteness of the Earth surface curvature yields the finite value for the magnetic inclination (dip) angle for which the signal wave transverses the ionospheric irregularity along the direction of larger spatial extension of this inhomogeneity even in the case of the horizontal propagation links. For the flat-geometry approximation, in contrast, the corresponding dip angle is equal to zero.

Another advantage of the proposed approach is that the phase screen used for simulation of action of the random ionosphere on the transmitting signal wave is set to be transversal to the propagation direction. This choice is quite natural and allows one to use the arbitrary propagation link geometries. It can be also compared with the choice of this plane to be parallel to the Earth surface in the flat-geometry approximation. The drawback of the latter choice is the need to use some projection transformations of the geometric parameters of the theory in order to include the slant propagation scenarios. In some cases, e.g. by considering the radio occultation applications, the flat-geometry approximation can be adopted for estimation of scintillation indices along the limb sounding links, cf. appendix in Ref. (Carrano et al., 2011). By doing so one should take care of proper interpretation of the rotation angles related to the magnetic inclination, magnetic declination, and tilt angles. In the presented approach we get rid of such extra complications by choosing the phase screen plane to be always transversal to the propagation direction. Moreover, the geometric parameters of the derived spectral model for the phase screen can be directly implemented in the scintillation simulation methods based on the multiple phase screens, e.g. in the GISM model (Béniguel, 2019).

The results of the current article can be also compared to the hybrid approach of Ref. (Priyadarshi & Wernik, 2013). These authors proposed to eliminate the divergencies of scintillation indices of very slant propagation links by modifying the receiver elevation angle. This modification is done in order to incorporate the difference in elevation angles of the scattering point and of the receiver appearing due to the sphericity of the Earth. The theoretical formulation of the problem within the approach of (Priyadarshi & Wernik, 2013) is due to Ref. (Rino, 1979a) and is thus still dependent on the flat-geometry assumption. We have shown that the approach of Ref. (Priyadarshi & Wernik, 2013) yields

divergence-free scintillation indices with the comparable values to those obtained within the spherical-geometry approximation but may define the regions of enhanced scintillation in parameter space that are displaced from those calculated within the proposed approach.

In this study we have ignored the morphology of the irregularity strength parameter integrated over the thickness of the irregular ionosphere. Therefore we have set $C_s\Delta h$=const in order to emphasize the purely geometric enhancement effect on scintillation levels. This morphology can be added within the WBMOD model according to Refs. (Fremouw & Secan, 1984; Secan et al., 1987, 1997) in order to obtain the global distribution of scintillation indices. One practically interesting example of geometrically enhanced scintillation is connected with the problem of the VHF signal propagation from a geostationary beacon satellite. If this satellite is located over the equator, the received signal exhibit strong scintillation at mid-latitudes, the effect reported in Ref. (Sinno & Minakoshi, 1983). In this region the integrated irregularity strength parameter attains almost constant and relatively low values, cf. Ref. (Rogers et al., 2014). So the characteristics that are associated with the level of disturbance of the ionospheric medium does not contribute to this scintillation enhancement effect. On the other hand, the proper accounting of the geometry of communication link and of the anisotropic field-aligned scintillation-associated irregularities allows one to explain the observed enhancement effect.

Appendix A Determination of coordinates of the scattering point

In most practical situations we know the geographic coordinates of the sender and the receiver but not those of the scattering point. Suppose we can estimate or determine the altitude of the scattering layer, h_p, i.e., by assuming that it coincides with the height of ionospheric pierce point. With this knowledge we are able to determine the geographic or local coordinates of the scattering point with the help of the procedure outlined in this appendix.

Let the position of the scattering point be given by the vector $\boldsymbol{r}_p$ in some conventional terrestrial coordinate system (CTS). Similarly, let the vectors $\boldsymbol{r}_s$ and $\boldsymbol{r}_r$ denote the positions of the sender and of the receiver, respectively. Denoting the Earth radius as $R_\oplus$ we have $|\boldsymbol{r}_p| = R_\oplus + h_p$. Similarly we have $|\boldsymbol{r}_s| = R_\oplus + h_s$ and $|\boldsymbol{r}_r| = R_\oplus + h_r$, where h_s and h_r are the altitudes of the sender and the receiver, correspondingly[5]. The orientation of the vectors $\boldsymbol{r}_s$, $\boldsymbol{r}_r$ in the CTS is described by the longitudes Λ_s, Λ_r and by the corresponding latitudes Φ_s, Φ_r. The corresponding coordinates Λ_p and Φ_p of the scattering point are to be determined.

We firstly obtain the expressions for the azimuth and zenith angles. We refer to Fig. A1 for necessary geometric constructions. The angle between the vectors $\boldsymbol{r}_s$ and $\boldsymbol{r}_r$ is obtained from the cosine law for spherical triangles as

$$\cos\delta = \sin\Phi_r \sin\Phi_s + \cos\Phi_r \cos\Phi_s \cos(\Lambda_s - \Lambda_r). \tag{A1}$$

From the triangle ORS of Fig. A1 (b) using the law of sines we derive

$$\frac{\sin\delta}{\ell} = \frac{\sin\theta_r}{|\boldsymbol{r}_s|}, \tag{A2}$$

where

$$\ell^2 = |\boldsymbol{r}_s|^2 + |\boldsymbol{r}_r|^2 - 2|\boldsymbol{r}_s||\boldsymbol{r}_r|\cos\delta \tag{A3}$$

[5] We preserve the finite value of the receiver altitude by keeping in mind potential applications to the limb sounding links, where both sender and receiver are satellites.

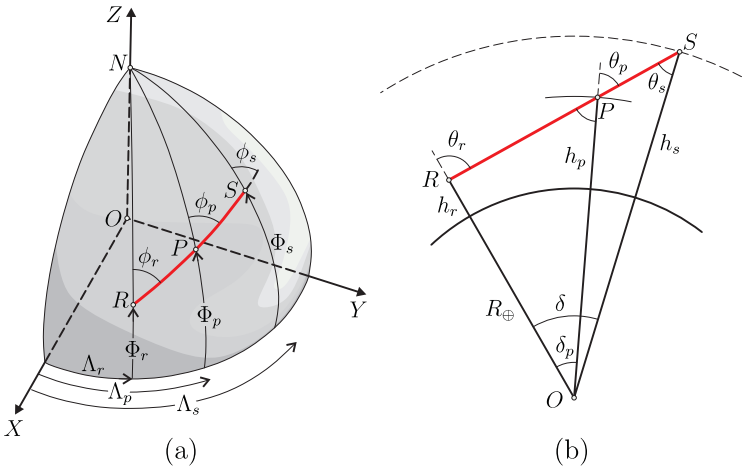

Figure A1. Geometric constructions used for the determination of: (a) the geographic coordinates Φ_p and Λ_p as well as of the azimuth angles ϕ_r, ϕ_p, ϕ_s associated with the slant path; (b) the zenith angles θ_r, θ_p, and θ_s.

is the slant range between the sender and the receiver. From the law of cosines for the triangle ORS we can also write

$$|\boldsymbol{r}_s|^2 = \ell^2 + |\boldsymbol{r}_r| + 2\ell|\boldsymbol{r}_r|\cos\theta_r. \tag{A4}$$

Substituting Eqs. (A2) and (A3) in Eq. (A4) one obtains for the receiver zenith angle the following expression:

$$\theta_r = \arctan\left(\frac{\sin\delta}{\cos\delta - \frac{|\boldsymbol{r}_r|}{|\boldsymbol{r}_s|}}\right) = \arctan\left(\frac{\sin\delta}{\cos\delta - \frac{R_\oplus + h_r}{R_\oplus + h_s}}\right) \tag{A5}$$

From the spherical triangle RNS on Fig. A1 (a) we obtain by using the sine and cosine theorems:

$$\begin{aligned} \frac{\sin\phi_r}{\sin\left(\frac{\pi}{2} - \Phi_s\right)} &= \frac{\sin(\Lambda_s - \Lambda_r)}{\sin\delta}, \\ \cos\left(\frac{\pi}{2} - \Phi_s\right) &= \cos\delta\sin\Phi_r + \sin\delta\cos\Phi_r\cos\phi_r \end{aligned} \tag{A6}$$

from which follows the expression for the azimuth angle for the link at the receiver location:

$$\phi_r = \arctan\left(\frac{\sin(\Lambda_s - \Lambda_r)\cos\Phi_r\cos\Phi_s}{\sin\Phi_s - \sin\Phi_r\cos\delta}\right). \tag{A7}$$

In the similar footing we obtain for the zenith angle of the link at the location of the scattering point

$$\theta_p = \arctan\left(\frac{\sin\theta_r}{\sqrt{\left(\frac{R_\oplus + h_p}{R_\oplus + h_r}\right)^2 - \sin^2\theta_r}}\right). \tag{A8}$$

For the azimuth angle at the scattering point location we use the half-angle formula for the spherical triangle RNP that yields

$$\phi_p = \pi - 2\arctan\left(\left\{\frac{\sin\left[\frac{1}{2}(\delta_p + \Phi_p - \Phi_r)\right]}{\sin\left[\frac{1}{2}(\delta_p - \Phi_p + \Phi_r)\right]}\frac{\cos\left[\frac{1}{2}(\delta_p + \Phi_p + \Phi_r)\right]}{\cos\left[\frac{1}{2}(\delta_p - \Phi_p - \Phi_r)\right]}\right\}^{\frac{1}{2}}\right), \tag{A9}$$

where

$$\delta_p = \theta_r - \theta_p \tag{A10}$$

is the angle between the vectors $\boldsymbol{r}_r$ and $\boldsymbol{r}_p$ and

$$\Phi_p = \frac{\pi}{2} - \arccos\left(\sin\Phi_r \cos\delta_p + \cos\Phi_r \sin\delta_p \cos\phi_r\right) \tag{A11}$$

is the geographic latitude at the scattering point. The latter expression is obtained from the cosine law for the spherical triangle RNP. Finally, using the cosine theorem for the spherical triangle RNP we obtain the geographic longitude of the scattering point as

$$\Lambda_p = \Lambda_r + \arctan\left(\frac{\sin\phi_r \sin\delta_p \cos\Phi_r}{\cos\delta_p - \sin\Phi_p \sin\Phi_r}\right). \tag{A12}$$

Equations (A8), (A9), (A11), (A12) determines the unknown geographic and local coordinates of the scattering point provided its height above the ground is known.

For the sake of completeness we also list the formulas for the zenith and azimuth angles of the link at the sender location. On the similar footing as the expressions (A5) and (A7) have been derived we obtain

$$\theta_s = \arctan\left(\frac{\sin\delta}{\frac{R_\oplus + h_s}{R_\oplus + h_r} - \cos\delta}\right), \tag{A13}$$

$$\phi_s = \arctan\left(\frac{\sin(\Lambda_s - \Lambda_r)\cos\Phi_r \cos\Phi_s}{\sin\Phi_s \cos\delta - \sin\Phi_r}\right), \tag{A14}$$

where δ is given in Eq. (A1).

We finally determine the distance between the scattering point and the receiver, which we denote $s = \overline{PR}$, cf. Fig. A1 (b). Using the cosine theorem for the triangle ORS we obtain

$$s = \sqrt{(R_\oplus + h_r)^2 + (R_\oplus + h_p)^2 - 2(R_\oplus + h_r)(R_\oplus + h_p)\cos\delta_p}, \tag{A15}$$

where δ_p is given by Eq. (A10).

Appendix B Calculation of autocorrelation function in the local coordinates of the receiver

The autocorrelation functions for the log-amplitude and phase fluctuations, cf. Eqs. (16), (17), have been obtained as the functions of the spatial coordinates associated with the direction of radio wave propagation. In this case the z variable is counted along the direction of propagation while the spatial variable $\boldsymbol{r}_\perp$ is transversal to this direction. The components of the vector $\boldsymbol{r}_\perp$ are defined in the xy coordinate plane, where the x-axis lies in the plane associated with the communication link, cf. Fig. 2. For the calculation of scintillation indices, the autocorrelation functions have been taken at $z = s$ and $\boldsymbol{r}_\perp = 0$ with s being the slant range from the scattering irregularity to the receiver station. If one is interested in the correlation analysis of the phase and log-amplitude fluctuations, the variable $\boldsymbol{r}_\perp$ should be kept finite. Moreover, the receiver of the signal usually performs the correlation analysis for quantities measured within the plane perpendicular to the local zenith direction. Thus, it is essential to perform transformation from variables $\boldsymbol{r}_\perp, z$ to the variables associated with the receiver correlation plane (Khudukon et al., 1994).

Let us consider for definiteness the correlation function for the log-amplitude fluctuations. Substituting Eq. (12) in Eq. (14) one obtains

$$\begin{aligned}\rho_\chi(\boldsymbol{r}_1, \boldsymbol{r}_2) &= \frac{k^2}{4\pi^2}\int \rho_{\delta\varphi}(\boldsymbol{r}'_{1,\perp} - \boldsymbol{r}'_{2,\perp})\frac{1}{z_1}\cos\Big(\frac{k}{2z_1}|\boldsymbol{r}_{1,\perp} - \boldsymbol{r}'_{1,\perp}|^2\Big) \\ &\times \frac{1}{z_2}\cos\Big(\frac{k}{2z_2}|\boldsymbol{r}_{2,\perp} - \boldsymbol{r}'_{2,\perp}|^2\Big)\mathrm{d}^2\boldsymbol{r}'_{1,\perp}\mathrm{d}^2\boldsymbol{r}'_{2,\perp}.\end{aligned} \tag{B1}$$

Using the spectral representation of the correlation function $\rho_{\delta\varphi}$ this integral can be reduced to the following form:

$$\rho_\chi(\boldsymbol{r}_\perp, z_1, z_2) = \frac{1}{2}\int \Phi_{\delta\varphi}(\boldsymbol{\kappa}_\perp)\, e^{i\boldsymbol{\kappa}_\perp\cdot\boldsymbol{r}_\perp}\Big[\cos\Big(\frac{z_1-z_2}{2k}\kappa_\perp^2\Big) - \cos\Big(\frac{z_1+z_2}{2k}\kappa_\perp^2\Big)\Big]\mathrm{d}^2\boldsymbol{\kappa}_\perp, \quad \text{(B2)}$$

where $\boldsymbol{r}_\perp = \boldsymbol{r}_{1,\perp} - \boldsymbol{r}_{2,\perp}$. The expression (B2) reduces to Eq. (16) by setting $z_1 = z_2 = s$.

Let us now express the autocorrelation (B2) in terms of the spatial variables defined in the conventional receiver coordinates. Let we define the NED coordinate system of the receiver as X, Y, Z and assume that one value of log-amplitude for correlation analysis is measured at the center of this coordinate system. This value is correlated then with the log-amplitude value measured in XY plane at the point which position is determined by the vector $\boldsymbol{R}_\perp$. Clearly, the vector $\boldsymbol{R}_\perp$ is the vector $\boldsymbol{r}_\perp$ projected on the plane XY. The components r_x, r_y of the vector $\boldsymbol{r}_\perp$ can be expressed in terms of the components of the vector $\boldsymbol{R}_\perp$ as

$$r_x = \cos\theta_r(R_X\cos\phi_r - R_Y\sin\phi_r), \qquad r_y = R_X\sin\phi_r + R_Y\cos\phi_r. \quad \text{(B3)}$$

Additionally to this, one needs to account now that $z_1 \neq z_2$ if we use the receiver plane for performing the correlation analysis. If z_1 is chosen to be equal to the slant range, i.e.,

$$z_1 = s, \quad \text{(B4)}$$

then the value of z_2 is determined as

$$z_2 = s + \sqrt{R_X^2 + R_y^2}\tan\omega, \quad \text{(B5)}$$

where

$$\omega = \arccos\left(\frac{\tau}{\sqrt{R_x^2+R_y^2}}\right), \quad \text{(B6)}$$

$$\tau = \sqrt{R_x^2(\cos^2\theta_r\cos^2\phi_r + \sin^2\phi_r) + R_y^2(\cos^2\theta_r\sin^2\phi_r + \cos^2\phi_r) + R_xR_y\sin^2\theta_r\sin 2\phi_r}$$

is the angle between the vectors $\boldsymbol{R}_\perp$ and $\boldsymbol{r}_\perp$. Substitution of Eqs. (B3)-(B5) in Eq. (B2) yields the expression of the log-amplitude correlation as the function of the distance vector defined in the receiver plane.

Appendix C Mapping function from vertical to slant propagation path lengths

In this appendix we derive the expression for the mapping function M that allows one to express the slant lengths in terms of the corresponding lengths defined along the vertical direction. Firstly, we derive the mapping function where the vertical direction is taken to be the vertical at the receiver location. In this case M is the function of the receiver zenith angle θ_r, since this angle defines how the slant path is inclined relative to the receiver vertical direction, cf. Fig. A1 (b). Using simple geometric considerations, the length element along the slant direction, $\mathrm{d}s$, can be expressed in terms of the length element along the receiver vertical, $\mathrm{d}z$, as

$$\mathrm{d}s = \frac{\mathrm{d}h}{\sqrt{1 - \left(\frac{R_\oplus + h_r}{R_\oplus + h}\right)^2\sin^2\theta_r}}, \quad \text{(C1)}$$

where for explanation of the notations we refer to Appendix A and Fig. A1 (b). We consider now the spherical shell of the thickness Δh with center at the center of the Earth. The outer radius of the shell is $R_\oplus + h_p$ and the inner radius is correspondingly $R_\oplus +$

$h_p - \Delta h$. The slant thickness of the shell along the path that connects the scattering point P and the receiver R follows from (C1) as

$$\Delta s = \int_0^{\Delta s} \mathrm{d}s = \int_{h_p-\Delta h}^{h_p} \frac{\mathrm{d}h}{\sqrt{1 - \left(\frac{R_\oplus + h_r}{R_\oplus + h}\right)^2 \sin^2\theta_r}}. \tag{C2}$$

Performing the integration in the right side of the equation, one obtains

$$\begin{aligned} \Delta s &= \Delta h \cdot M(\theta_r), \\ M(\theta_r) &= \sqrt{\xi^2\cos^2\theta_r + 2\xi\zeta + \zeta^2} - \sqrt{\xi^2\cos^2\theta_r + 2\xi(\zeta-1) + (\zeta-1)^2}, \end{aligned} \tag{C3}$$

where $\xi = (R_\oplus + h_r)/\Delta h$ and $\zeta = (h_p - h_r)/\Delta h$.

Here we also derive the expression for M as the function of the zenith angle of the scattering point θ_p. Applying the sine theorem to the triangle ORP on Fig. A1 (b), one obtains

$$\cos\theta_r^2 = 1 - \left(\frac{R_\oplus + h_p}{R_\oplus + h_r}\right)^2 \sin^2\theta_p. \tag{C4}$$

Inserting this equation in Eq. (C3) one derives

$$\begin{aligned} \Delta s &= \Delta h \cdot M(\theta_p), \\ M(\theta_p) &= \tilde{\xi}\cos\theta_p - \sqrt{\tilde{\xi}^2\cos^2\theta_p - 2\tilde{\xi} + 1}, \end{aligned} \tag{C5}$$

where $\tilde{\xi} = (R_\oplus + h_p)/\Delta h$. Here we note that while the zenith angle of the receiver is defined in the range $[0, \pi/2]$, the zenith angle at the scattering point at the same time varies in the range $[0, \theta_p^{\max}]$, where

$$\theta_p^{\max} = \arccos\left(\tilde{\xi}^{-1}\sqrt{2\tilde{\xi} - 1}\right). \tag{C6}$$

The maximal slant thickness of the spherical shell at this angle is

$$\Delta s^{\max} = \sqrt{\Delta h^2 + 2\Delta h\,(R_\oplus + h_p - \Delta h)}.$$

In order to complete the discussion of the mapping functions, we express the slant range s in terms of the receiver zenith angle and in terms of the vertical height from the receiver to the scattering point, i.e., in terms of $h_p - h_r$. This dependence can be again represented in terms of the mapping function $\overline{M}$, where

$$\begin{aligned} s &= (h_p - h_r)\cdot\overline{M}(\theta_r), \\ \overline{M}(\theta_r) &= \sqrt{\overline{\xi}^2\cos^2\theta_r + 2\overline{\xi} + 1} - \overline{\xi}\cos\theta_r, \qquad \overline{\xi} = (R_\oplus + h_r)/(h_p - h_r), \end{aligned} \tag{C7}$$

which one obtains directly from Eq. (C5) via the replacement $\Delta h \rightarrow h_p - h_r$. Similarly, Eq. (C5) can be used to express the slant range in terms of the zenith angle of the scattering point. The slant range representation (C7) is an alternative to the formula (A15).

Appendix D On the relationship between power spectral power densities $\Phi_{\delta\varphi}$ and $\Phi_{\delta N_e}$.

In this appendix we derive Eq. (18) and comment on the analogous relationship for the case of the plan-parallel ionosphere. Consider the correlation function of phase fluctuations of the phase screen determined at two spatial points. The positions of the points are given by the vectors $\boldsymbol{r}_{1,\perp}$ and $\boldsymbol{r}_{2,\perp}$ that lie in the plane of the phase screen

and with the origins at the cross-section point of the signal ray and the phase screen. In the following we assume that the medium is spatially homogeneous. Substituting Eq. (8) in Eq. (14) and denoting $\boldsymbol{r}_\perp = \boldsymbol{r}_{1,\perp} - \boldsymbol{r}_{2,\perp}$ we obtain

$$\rho_{\delta\varphi}(\boldsymbol{r}_\perp) = \lambda^2 r_e^2 \int_0^{\Delta s}\int_0^{\Delta s} \rho_{\delta N_e}(\boldsymbol{r}_\perp, z_1 - z_2)\mathrm{d}z_1\mathrm{d}z_2, \tag{D1}$$

where Δs is the slant thickness of the ionospheric layer. Transforming the integration variables according to $z = z_1 - z_2$, $Z = (z_1 + z_2)/2$ one can perform the integration over Z variable explicitly. Using the spectral representation of the correlation functions in Eq. (D1) one derives

$$\int_{\mathbb{R}^2} \Phi_{\delta\varphi}(\boldsymbol{\kappa}_\perp) e^{i\boldsymbol{\kappa}_\perp\cdot\boldsymbol{r}_\perp}\mathrm{d}^2\boldsymbol{\kappa}_\perp = \lambda^2 r_e^2\,\Delta s \int_{-\Delta s}^{\Delta s}\int_{\mathbb{R}^3} \Phi_{\delta N_e}(\boldsymbol{\kappa}_\perp, \kappa_z) e^{i\boldsymbol{\kappa}_\perp\cdot\boldsymbol{r}_\perp + i\kappa_z z}\mathrm{d}z\,\mathrm{d}^2\boldsymbol{\kappa}_\perp\,\mathrm{d}\kappa_z, \tag{D2}$$

where the slant thickness of the spherical shell Δs is related to the shell thickness with the help of the mapping function as given in Eqs. (C3) and (C5). Integration of Eq. (D2) with respect to κ_z yields then the required formula (18).

For the plan-parallel model of the ionospheric layer considered in (Rino & Fremouw, 1977; Rino, 1979a) the equation (D2) can be written as

$$\begin{aligned}&\int_{\mathbb{R}^2} \Phi_{\delta\varphi}(\boldsymbol{K}_\perp) e^{i\boldsymbol{K}_\perp\cdot\boldsymbol{R}_\perp}\mathrm{d}^2\boldsymbol{K}_\perp \\ &= \lambda^2 r_e^2\,\Delta s \int_{-\Delta s}^{\Delta s}\int_{\mathbb{R}^3} \Phi_{\delta N_e}(\boldsymbol{K}_\perp, K_h) e^{i\boldsymbol{K}_\perp\cdot(\boldsymbol{R}_\perp + \tan\theta\boldsymbol{a}_{k,\perp}h)} e^{iK_h h}\mathrm{d}(h\sec\theta)\,\mathrm{d}^2\boldsymbol{K}_\perp\mathrm{d}K_h,\end{aligned} \tag{D3}$$

where $\boldsymbol{R}_\perp$ is the spatial vector lying in the plane of the ground observer, cf. Appendix B, h is the spatial variable counted along the receiver vertical starting from the position of the scattering point, and $\boldsymbol{a}_{k,\perp} = \sin\theta(\cos\phi \quad \sin\phi)^T$ is the transversal component of the unit vector $\boldsymbol{a} = \boldsymbol{k}/k$ with $\boldsymbol{k}$ being the wave vector of the signal wave. It is worth to note that due to the flat geometry, the zenith, θ, and azimuth, ϕ, angles for the sender, scattering point, and receiver attain the same values in contrast to the case of the spherical geometry. The slant thickness of the plan-parallel ionospheric slab is $\Delta s = \Delta h \sec\theta$ with Δh being the slab thickness. The shift of the spatial vector $\boldsymbol{R}_\perp$ to $\boldsymbol{R}_\perp + \tan\theta\boldsymbol{a}_{k,\perp}h$ accounts the shift of the center of the receiver coordinate system relative to the projection of the scattering point on the flat-Earth surface.

Integration of Eq. (D3) with respect to h and K_h yields

$$\Phi_{\delta\varphi}(\boldsymbol{K}_\perp) = 2\pi\lambda^2 r_e^2 \Delta h (\sec\theta)^2 \Phi_{\delta N_e}(\boldsymbol{K}_\perp, -\tan\theta\boldsymbol{K}_\perp\cdot\boldsymbol{a}_{k,\perp}). \tag{D4}$$

If we compare Eq. (D4) with Eq. (18), we observe that the constant factors on the right hand sides of these equations have different dependencies on the horizontal-to-slant mapping functions. In the case of the spherical geometry this factor is proportional to the mapping function (C3) [alternatively given by Eq. (C5)], while for the flat geometry this factor is proportional to the second power of the corresponding mapping function, i.e., to $(\sec\theta)^2$.

Another observation is on the manner of how the two-dimensional power spectral density for phase fluctuation is related to the three-dimensional spectrum of electron density fluctuations in different geometries. As has been discussed in Sec. 4 we associate certain ellipsoidal surface with the three-dimensional PSD in spatial frequency space for anisotropic electron density fluctuations. The corresponding two-dimensional PSD for a phase screen within the spherical-geometry approximation depends on the quadratic form (ellipse) that

is formed by crossing the ellipsoid with the plane of the phase screen. The latter is transversal to the propagation direction and is characterized by the condition κ_z=0. In the flat-geometry approximation, the cross-secting plane is perpendicular to the receiver vertical direction and the corrections for the elevated wave propagation path are incorporated in the formula by adjusting the position of this plane along the vertical coordinate by the value $\tan\theta \boldsymbol{K}_\perp \cdot \boldsymbol{a}_{k,\perp}$. Such corrections are of course unsatisfactory for the very slant propagation paths due to their divergent behavior.

Appendix E Calculation of integrals in Eqs. (34) and (35)

The integrals appearing in Eqs. (34), (35) have been calculated in (Rino, 1979a). In the sake of completeness we outline the integration procedure in this appendix.

Consider firstly the integral

$$\mathcal{I}_1 = \int\limits_{\mathbb{R}^2} \frac{\mathrm{d}\kappa_x\,\mathrm{d}\kappa_y}{\Big(\mathcal{A}\kappa_x^2 + 2\mathcal{B}\kappa_x\kappa_y + \mathcal{C}\kappa_y^2 + r_0^2\kappa_0^2\Big)^{\frac{p+2}{2}}}. \tag{E1}$$

We now perform the coordinate transformation in Eq. (E1) that brings the quadratic form (30) to the diagonal representation according to:

$$\begin{aligned} \kappa_x &= \frac{\mathcal{A}-\mathcal{C}+\mathcal{D}}{2\sqrt{\mathcal{B}\mathcal{D}}} q_x + \frac{\mathcal{A}-\mathcal{C}-\mathcal{D}}{2\sqrt{\mathcal{B}\mathcal{D}}} q_y, \\ \kappa_y &= \sqrt{\frac{\mathcal{B}}{\mathcal{D}}}(q_x+q_y), \end{aligned} \tag{E2}$$

where $\mathcal{D} = \sqrt{(\mathcal{A}-\mathcal{C})^2 + 4\mathcal{B}^2}$. The Jacobian of this transformation is equal to one. The integral (E1) can be written in terms of the new variables as

$$\mathcal{I}_1 = \int\limits_{\mathbb{R}^2} \frac{\mathrm{d}q_x\,\mathrm{d}q_y}{\Big(aq_x^2 + bq_y^2 + r_0^2\kappa_0^2\Big)^{\frac{p+2}{2}}}, \tag{E3}$$

where

$$\begin{aligned} a &= \tfrac{1}{2\mathcal{B}}\Big[2\mathcal{B}^2 + \mathcal{A}\Big(\mathcal{A}-\mathcal{C}+\mathcal{D}\Big)\Big], \\ b &= -\tfrac{1}{2\mathcal{B}}\Big[2\mathcal{B}^2 + \mathcal{A}\Big(\mathcal{A}-\mathcal{C}-\mathcal{D}\Big)\Big]. \end{aligned} \tag{E4}$$

By rescaling the integration variables and switching to the polar coordinates this integral can be reduced to

$$\mathcal{I}_1 = \frac{\pi}{\sqrt{\mathcal{A}\mathcal{C}-\mathcal{B}^2}} \int\limits_0^\infty \Big(x + r_0^2\kappa_0^2\Big)^{-\frac{p+2}{2}}\,\mathrm{d}x = \frac{2\pi}{\sqrt{\mathcal{A}\mathcal{C}-\mathcal{B}^2}} \frac{1}{p}(r_0\kappa_0)^{-p}. \tag{E5}$$

Inserting Eq. (E5) in (34) yields the phase scintillation index (36).

We now switch to the calculation of the integral

$$\mathcal{I}_2 = \int_{\mathbb{R}^2} \frac{\sin^2\Big[s(\kappa_x^2+\kappa_y^2)/2k\Big]}{\Big(\mathcal{A}\kappa_x^2 + 2\mathcal{B}\kappa_x\kappa_y + \mathcal{C}\kappa_y^2\Big)^{\frac{p+2}{2}}}\mathrm{d}\kappa_x\mathrm{d}\kappa_y \tag{E6}$$

which is used for calculation of the amplitude scintillation index (37). Performing the variable transformation (Appendix E) this integral is modified to

$$\mathcal{I}_2 = \int\limits_{\mathbb{R}^2} \frac{\sin^2\Big[s\big(\underline{a}q_x^2 + \underline{b}q_y^2\big)/2k\Big]\,\mathrm{d}q_x\,\mathrm{d}q_y}{\Big(aq_x^2 + bq_y^2\Big)^{\frac{p+2}{2}}}, \tag{E7}$$

where

$$\begin{aligned} \underline{a} &= \tfrac{1}{2\mathcal{B}}\Big(\mathcal{D}+\mathcal{A}-\mathcal{C}\Big), \\ \underline{b} &= \tfrac{1}{2\mathcal{B}}\Big(\mathcal{D}-\mathcal{A}+\mathcal{C}\Big). \end{aligned} \tag{E8}$$

Performing the rescaling of the variables $q'_x = \underline{a}q_x$, $q'_y = \underline{b}q_y$ and using the polar coordinates the integral can be written as

$$\mathcal{I}_2 = \frac{1}{2}\int\limits_0^\infty t^{-\frac{p}{2}-1}\sin^2\Big(\frac{s\,t}{2k}\Big)\mathrm{d}t \int\limits_0^{2\pi} \frac{\mathrm{d}\phi}{\Big(\frac{a}{\underline{a}} - \Big(\frac{a}{\underline{a}} - \frac{b}{\underline{b}}\Big)\sin^2\phi\Big)^{\frac{p+2}{2}}}. \tag{E9}$$

Integrating over t one obtains after some simplifications (Prudnikov et al., 1992):

$$\mathcal{I}_2 = \frac{\sqrt{\pi}}{2}\Big(\frac{s}{2k}\Big)^{\frac{p}{2}}\frac{1}{p}\frac{\Gamma\Big(1-\frac{p}{4}\Big)}{\Gamma\Big(\frac{1}{2}+\frac{p}{4}\Big)} \int\limits_0^{2\pi} \frac{\mathrm{d}\phi}{\Big(\frac{1}{2}\Big(\mathcal{A}+\mathcal{C}+\mathcal{D}\Big) - \mathcal{D}\sin^2\phi\Big)^{\frac{p+2}{2}}}. \tag{E10}$$

Changing the integration variable as $x = \sin^2\phi$ one can see that the integral attains the form of the Euler integral representation of the hypergeometric function ${}_2F_1(a,b;c;z)$

$$\mathcal{I}_2 = \pi^{\frac{3}{2}}\Big(\frac{s}{2k}\Big)^{\frac{p}{2}}\frac{1}{p}\frac{\Gamma\Big(1-\frac{p}{4}\Big)}{\Gamma\Big(\frac{1}{2}+\frac{p}{4}\Big)}\Big[\frac{1}{2}\Big(\mathcal{A}+\mathcal{B}+\mathcal{C}\Big)\Big]^{-\frac{p+2}{2}}{}_2F_1\Big(\frac{p+2}{2},\frac{1}{2};1;\frac{2\mathcal{D}}{\mathcal{A}+\mathcal{C}+\mathcal{D}}\Big). \tag{E11}$$

Using the Euler transformation ${}_2F_1(a,b;c;z) = (1-z)^{c-a-b}{}_2F_1(c-a,c-b;c;z)$ and the formula

$${}_2F_1(a,b;c;z) = 2^{2b-1}\Gamma(b+1/2)z^{\frac{1}{2}-b}(1-z)^{(2b-2a-1)/4}P^{1/2-b}_{a-b-1/2}\Big(\frac{2-z}{2\sqrt{1-z}}\Big),$$

where $P^{\beta}_{\alpha}(z)$ is the Legendre function, equation (E11) can be written in the form

$$\mathcal{I}_2 = \pi^{\frac{3}{2}}\Big(\frac{s}{2k}\Big)^{\frac{p}{2}}\frac{1}{p}\frac{\Gamma\Big(1-\frac{p}{4}\Big)}{\Gamma\Big(\frac{1}{2}+\frac{p}{4}\Big)}\left(\frac{1}{\sqrt{\mathcal{AC}-\mathcal{B}^2}}\right)^{\frac{p+2}{2}}P_{\frac{p}{2}}\Big(\frac{\mathcal{A}+\mathcal{C}}{2\sqrt{\mathcal{AC}-\mathcal{B}^2}}\Big). \tag{E12}$$

This result is used for calculation of the scintillation index given by Eq. (37).

Acknowledgments

The work was carried out within the programmatic funding of the German Aerospace Center.

References

Afraimovich, E. L., Ishin, A. B., Tinin, M. V., Yasyukevich, Y. V., & Jin, S. G. (2011). First evidence of anisotropy of GPS phase slips caused by the mid-latitude field-aligned ionospheric irregularities. *Adv. Space. Res.*, *47*, 1674-1680. doi: http://dx.doi.org/10.1016/j.asr.2011.01.015

Alken, P., Thébault, E., Beggan, C. D., Amit, H., Aubert, J., Baerenzung, J., ... Zhou, B. (2021). International Geomagnetic Reference Field: the thirteenth generation. *Earth, Planets and Space*, *73:49*, 1-25. doi: http://dx.doi.org/10.1186/s40623-020-01288-x

Anderson, P. C., & Straus, P. R. (2005). Magnetic field orientation control of GPS occultation observations of equatorial scintillation. *Geophys. Res. Lett.*, *32*, L21107. doi: http://dx.doi.org/10.1029/2005GL023781

Atilaw, T. Y., Cilliers, P., & Martinez, P. (2017). Azimuth-dependent elevation threshold (ADET) masks to reduce multipath errors in ionospheric studies using GNSS. *Adv. Space Res.*, *59*, 2726-2739. doi: http://dx.doi.org/10.1016/j.asr.2016.10.021

Banville, S., & Langley, R. B. (2013). Mitigating the impact of ionospheric cycle slips in GNSS observations. *J. Geodet.*, *87*, 179-193. doi: http://dx.doi.org/10.1007/s00190-012-0604-1

Belcher, D. P., Mannix, C. R., & Cannon, P. S. (2017). Measurement of the ionospheric scintillation parameter C_kL from SAR images of clutter. *IEEE Trans. Geosci. Remote Sens.*, *55*, 5937 - 5943. doi: http://dx.doi.org/10.1109/TGRS.2017.2717081

Béniguel, Y. (2019). Ionospheric scintillations: indices and modeling. *Radio Sci.*, *54*, 618-632. doi: http://dx.doi.org/10.1029/2018RS006655

Bezler, I. V., Ishin, A. B., Konetskaya, E. V., & Tinin, M. V. (2019). Effect of anisotropy of ionospheric inhomogeneities in the detection of faults in phase GNSS measurements. *Geomagnetism and Aeronomy*, *59*, 342-350. doi: http://dx.doi.org/10.1134/S0016793219030046

Bhattacharyya, A., Yeh, K. C., & Franke, S. J. (1992). Deducing turbulence parameters from transionospheric scintillation measurements. *Space Sci. Rev.*, *61*, 335-386. doi: http://dx.doi.org/10.1007/BF00222311

Booker, H. G. (1956). A theory of scattering by nonisotropic irregularities with application to radar reflections from the aurora. *J. Atm. Terr. Phys.*, *8*, 204-221. doi: http://dx.doi.org/10.1016/0021-9169(56)90126-X

Booker, H. G., Ratcliffe, J. A., & Shinn, D. H. (1950). Diffraction from an irregular screen with applications to ionospheric problems. *Phil. Trans. Roy. Soc.*, *A 242*, 579-607. doi: http://dx.doi.org/10.1098/rsta.1950.0011

Briggs, B. H., & Parkin, I. A. (1963). On the variation of radio star and satellite scintillations with zenith angle. *J. Atm. Terr. Phys.*, *25*, 339-366. doi: http://dx.doi.org/10.1016/0021-9169(63)90150-8

Briggs, B. H., Phillips, G. J., & Shinn, D. H. (1950). The analysis of observations on spaced receivers of the fading of radio signals. *Proc. Phys. Soc. B*, *63*, 106-121. doi: http://dx.doi.org/10.1088/0370-1301/63/2/305

Camps, A., Park, H., Foti, G., & Gommenginger, C. (2016). Ionospheric effects in GNSS-reflectometry from space. *IEEE J. of Select. Topics in Appl. Earth Obs. and Remote Sensing*, *9*, 5851 - 5861. doi: http://dx.doi.org/10.1109/JSTARS.2016.2612542

Carrano, C. S., Groves, K. M., & Caton, R. G. (2012). Simulating the impacts of ionospheric scintillation on L band SAR image formation. *Radio Sci.*, *47*, RS0L20. doi: http://dx.doi.org/10.1029/2011RS004956

Carrano, C. S., Groves, K. M., Caton, R. G., Rino, C. L., & Straus, P. R. (2011). Multiple phase screen modeling of ionospheric scintillation along radio occultation raypaths. *Radio Sci.*, *46*, RS0D07. doi: http://dx.doi.org/10.1029/2010RS004591

Carrano, C. S., Groves, K. M., & Rino, C. L. (2019). On the relationship between the rate of change of total electron content index (ROTI), irregularity s trength (C_kL), and the scintillation index (S_4). *J. Geophys. Res.*, *124*, 2099-2112. doi: http://dx.doi.org/10.1029/2018JA026353

Carter, B. A., Retterer, J. M., Yizengaw, E., Wiens, K., Wing, S., Groves, K., ... Zhang, K. (2014). Using solar wind data to predict daily GPS scintillation occurrence in the African and Asian low-latitude regions. *Geophys. Res. Lett.*, *41*, 8176–8184. doi: http://dx.doi.org/10.1002/2014GL062203

Cervera, M. A., Thomas, R. M., Groves, K. M., Ramli, A. G., & Effendy. (2001). Validation of WBMOD in the Southeast Asian region. *Radio Sci.*, *36*, 1559-1572. doi: http://dx.doi.org/10.1029/2000RS002520

Clifford, S. F., & Yura, H. T. (1974). Equivalence of two theories of strong optical

scintillation. *J. Opt. Soc. Am.*, *64*, 1641-1644. doi: http://dx.doi.org/10.1364/JOSA.64.001641

Conroy, J. P., Deshpande, K., Kunduri, B., Varney, R. H., Scales, W., & Zaghloul, A. (2021). Ionospheric scintillation data inversion to characterize the structures associated with a series of polar cap patches. *Radio Sci.*, *56*, e2020RS007235. doi: http://dx.doi.org/10.1029/2020RS007235

Conroy, J. P., Deshpande, K., Scales, W., & Zaghloul, A. (2022). Statistical analysis of refractive and diffractive scintillation at high latitudes. *Radio Sci.*, *57*, e2021RS007259. doi: http://dx.doi.org/10.1029/2021RS007259

Crane, R. K. (1977). Ionospheric scintillation. *Proc. IEEE*, *65*, 180-199. doi: http://doi.org/10.1109/PROC.1977.10456

De Michelis, P., Consolini, G., Pignalberi, A., Tozzi, R., Coco, I., Giannattasio, F., ... Balasis, G. (2021). Looking for a proxy of the ionospheric turbulence with Swarm data. *Sci. Rep.*, *11*, 6183. doi: http://dx.doi.org/10.1038/s41598-021-84985-1

De Wolf, D. A. (1974). Waves in turbulent air: A phenomenological model. *Proc. IEEE*, *62*, 1523-1529. doi: http://dx.doi.org/10.1109/PROC.1974.9659

Dielacher, A., Fragner, H., & Koudelka, O. (2022). PRETTY – passive GNSS-Reflectometry for CubeSats. *Elektrotech. Inftech.*, *139*, 25-32. doi: http://dx.doi.org/10.1007/s00502-022-00993-7

Dyson, P. L., McClure, J. P., & Hanson, W. B. (1974). In situ measurements of the spectral characteristics of F region ionospheric irregularities. *J. Geophys. Res.*, *79*, 1497-1502. doi: http://dx.doi.org/10.1029/JA079i010p01497

El-Arini, M. B., Conker, R. S., Albertson, T. W., Reagan, J. K., Klobuchar, J. A., & Doherty, P. H. (1994). Comparison of real-time ionospheric algorithms for a GPS Wide-Area Augmentation System (WAAS). *Navigation*, *41*, 393-414. doi: http://dx.doi.org/10.1002/j.2161-4296.1994.tb01887.x

Fante, R. L. (1975a). Electromagnetic beam propagation in turbulent medium. *Proc. IEEE*, *63*, 1669-1692. doi: \http://dx.doi.org/10.1109/PROC.1975.10035

Forte, B., & Radicella, S. M. (2004). Geometrical control of scintillation indices: What happens for GPS satellitess. *Radio Sci.*, *39*, RS5014. doi: http://dx.doi.org/10.1029/2002RS002852

Forte, B., & Radicella, S. M. (2005). Comparison of ionospheric scintillation models with experimental data for satellite navigation applications. *Ann. Geophys.*, *48*, 505-514. doi: http://dx.doi.org/10.4401/ag-3215

Fremouw, E. J., & Larsinger, J. M. (1981). Recent high-latitude improvements in a computer-based scintillation model. In J. M. Goodman, F. D. Clarke, & J. Aarons (Eds.), *Effect of the ionosphere on radiowave systems* (p. 141-154). Naval Research Lab, Washington DC.

Fremouw, E. J., & Secan, J. A. (1984). Modeling and scientific application of scintillation results. *Radio Sci.*, *19*, 687-694. doi: http://dx.doi.org/10.1029/RS019i003p00687

Gola, M., Wernik, A. W., Franke, S. J., Liu, C. H., & Yeh, K. C. (1992). Behaviour of HILAT scintillation over Spitsbergen. *J. Atm. Terr. Phys.*, *54*, 1207-1213. doi: http://dx.doi.org/10.1016/0021-9169(92)90146-C

Helmboldt, J. F., & Zabotin, N. (2022). An observed trend between mid-latitudes km-scale irregularities and medium-scale traveling ionospheric disturbances. *Radio Sci.*, *57*, e2021RS007396. doi: http://dx.doi.org/10.1029/2021RS007396

Hewish, A. (1951). The diffraction of radio waves in passing through a phase-changing ionosphere. *Proc. Roy. Soc.*, *A 209*, 81-96. doi: http://dx.doi.org/10.1098/rspa.1951.0189

Hong, J., Chung, J.-K., Kim, Y. H., Park, J., Kwon, H.-J., Kim, J.-H., ... Kwak, Y.-S. (2020). Characteristics of ionospheric irregularities using GNSS scintillation indices measured at Jang Bogo Station, Antarctica (74.62°S,

4164.22°E). *Space Weather*, *18*, e2020SW002536. doi: http://dx.doi.org/10.1029/2020SW002536

Jandieri, G., Ishimaru, A., Rawat, B., Kharshiladze, O., & Diasamidze, Z. (2017). Power spectra of ionospheric scintillations. *Adv. Electromagn.*, *6*, 43-51. doi: http://dx.doi.org/10.7716/aem.v6i4.652

Ji, Y., Dong, Z., Zhang, Y., Zhang, Q., Yu, L., & Qin, B. (2022). Measuring ionospheric scintillation parameters from SAR images using phase gradient autofocus: A case study. *IEEE Trans. geosci. Remote Sens.*, *60*, 5200212. doi: http://dx.doi.org/10.1109/TGRS.2020.3044657

Ji, Y., Zhang, Q., Zhang, Y., Dong, Z., & Yao, B. (2020). Spaceborne P-band SAR imaging degradation by anisotropic ionospheric irregularities: A comprehensive numerical study. *IEEE Ztans. Geosci. Remote Sens.*, *58*, 5516-5526. doi: http://dx.doi.org/10.1109/TGRS.2020.2966710

Kelley, M. C., Pfaff, R., Baker, K. D., Ulwick, J. C., Livingston, R., Rino, C., & Tsunoda, R. (1982). Simultaneous rocket probe and radar measurements of equatorial spread f—transitional and short wavelength results. *J. Geophys. Res.*, *87*, 1575-1588. doi: http://dx.doi.org/10.1029/JA087iA03p01575

Kersley, L., Pryse, S. E., & Wheadon, N. S. (1988). Amplitude and phase scintillation at high latitudes over northern europe. *Radio Sci.*, *23*, 320-330. doi: http://dx.doi.org/10.1029/RS023i003p00320

Khudukon, B. Z., Tereshchenko, E. D., Galinov, A. V., Popov, A. A., & Nygrén, T. (1994). Determination of drift velocity and anisotropy of irregularities in the auroral ionosphere using radio source scintillation. *J. Atm. Terr. Phys.*, *56*, 93-102. doi: http://dx.doi.org/10.1016/0021-9169(94)90179-1

Knight, M., Cervera, M., & Finn, A. (1999). *A comparison of predicted and measured GPS performance in an ionospheric scintillation environment.* Nashville, TN.

Koster, J. R. (1963). Some measurements of the irregularities giving rise to radiostar scintillations at the equator. *J. Geophys. Res.*, *68*, 2579-2590. doi: http://dx.doi.org/10.1029/JZ068i009p02579

Koster, J. R. (1972). Equatorial scintillation. *Planetary Space Sci.*, *20*, 1999-2014. doi: http://dx.doi.org/10.1016/0032-0633(72)90056-6

Kravtsov, Y. A. (1970). Geometric depolarization of light in a turbulent atmosphere. *Radiophys. Quantum Electron.*, *13*, 217–220. doi: http://doi.org/10.1007/BF01031535

Kumagai, H., & Ogawa, T. (1986). Behavior of mid-latitude F-region irregularities deduced from spaced-receiver VHF scintillation measurements. *Radio Sci.*, *48*, 221-230. doi: http://dx.doi.org/10.1016/0021-9169(86)90097-8

Lay, E. H., Parker, P. A., Light, M., Carrano, C. S., Debchoudhury, S., & Haaser, R. A. (2018). Midlatitude ionospheric irregularity spectral density as determined by ground-based GPS receiver networks . *J. Space Weather Space Clim.*, *123*, 5055-5067. doi: http://dx.doi.org/10.1029/2018JA0253646

Li, C., Hancock, C. M., Veettil, S. V., Zhao, D., Galera Monico, J. F., & Hamm, N. A. S. (2022). Distinguishing ionospheric scintillation from multipath in GNSS signals using geodetic receivers. *GPS Solutions*, *26*, 150. doi: http://dx.doi.org/10.1007/s10291-022-01328-x

Li, Y., Hu, C., Ao, D., Dong, X., Tian, W., Li, S., & Hu, J. (2018). Ionospheric scintillation impacts on L-band geosynchronous D-InSAR system: models and analysis. *IEEE J. Sel. Top. Appl. Earth Obs. Remote Sens.*, *11*, 4862-4873. doi: http://dx.doi.org/10.1109/JSTARS.2018.2875384

Linty, N., Minetto, A., Dovis, F., & Spogli, L. (2018). Effects of phase scintillation on the GNSS positioning error during the September 2017 storm at Svalbard. *Space Weather*, *16*, 1317-1329. doi: http://dx.doi.org/10.1029/2018SW001940

Liu, Y., Zhou, C., Xu, T., Tang, Q., Deng, Z., Chen, G., & Wang, Z. (2021).

Review of ionospheric irregularities and ionospheric electrodynamic coupling in the middle latitude region. *Earth Planet. Sci.*, *5*, 462-482. doi: http://dx.doi.org/10.26464/epp2021025

Ludwig−Barbosa, V., Sievert, T., Rasch, J., Carlström, A., Pettersson, M. I., & Vu, V. T. (2020). Evaluation of ionospheric scintillation in GNSS radio occultation measurements and simulations. *Radio Sci.*, *55*, e2019RS006996. doi: http://dx.doi.org/10.1029/2019RS006996

MacDougall, J., & Eadie, D. C. (2005). The shape of midlatitude scintillation irregularities. *J. Atm. Solar-Terr. Phys.*, *67*, 931-935. doi: http://dx.doi.org/10.1016/j.jastp.2005.02.007

Mevius, M., van der Tol, S., Pandey, V. N., Vedantham, H. K., Brentjens, M. A., de Bruyn, A. G., ... Zaroubi, S. (2016). Probing ionospheric structures using the LOFAR radio telescope. *Radio Sci.*, *51*, 927-941. doi: http://dx.doi.org/10.1002/2016RS006028

Meyer, F. J., Chotoo, K., Chotoo, S. D., Huxtable, B. D., & Carrano, C. S. (2016). The influence of equatorial scintillation on L-band SAR image quality and phase. *IEEE Trans. Geosci. Remote Sens.*, *54*, 869 - 880. doi: http://dx.doi.org/10.1109/TGRS.2015.2468573

Mikkelsen, I. S., Aarons, J., & Martin, E. (1978). Geometrical considerations of 136 MHz amplitude scintillation in the auroral oval. *J. Atm. Terr. Phys.*, *40*, 479-483. doi: http://dx.doi.org/10.1016/0021-9169(78)90181-2

Mohanty, S., Carrano, C. S., & Singh, G. (2019). Effect of anisotropy on ionospheric scintillations observed by SAR. *IEEE Trans. Geosci. Remote Sens.*, *57*, 6888-6899. doi: http://dx.doi.org/10.1109/TGRS.2019.2909078

Mohanty, S., Singh, G., Carrano, C. S., & Sripathi, S. (2018). Ionospheric scintillation observation using space-borne synthetic aperture radar data. *Radio Sci.*, *53*, 1187-1202. doi: http://dx.doi.org/10.1029/2017RS006424

Moorcroft, D. R., & Arima, K. S. (1972). The shape of the F-region irregularities which produce satellite scintillations – Evidence for axial asymmetry. *J. Atm. Terr. Phys.*, *34*, 437-450. doi: http://dx.doi.org/10.1016/0021-9169(72)90045-1

Phelps, A. D. R., & Sagalyn, R. C. (1976). Plasma density irregularities in the high-latitude top side ionosphere. *J. Geophys. Res.*, *81*, 515-523. doi: http://dx.doi.org/10.1029/JA081i004p00515

Portillo, A., Herraiz, M., Radicella, S. M., & Ciraolo, L. (2008). Equatorial plasma bubbles studied using African slant total electron content observations. *J. Atm. Solar-Terr. Phys.*, *70*, 907-917. doi: http://dx.doi.org/10.1016/j.jastp.2007.05.019

Prikryl, P., Ghoddousi-Fard, R., Weygand, J. M., Viljanen, A., Connors, M., Danskin, D. W., ... Sreeja, V. (2016). GPS phase scintillation at high latitudes during the geomagnetic storm of 17–18 March 2015. *J. Geophys. Res.*, *121*, 10,448-10,465. doi: http://dx.doi.org/10.1002/2016JA023171

Prikryl, P., Jayachandran, P. T., Mushini, S. C., & Chadwick, R. (2011). Climatology of GPS phase scintillation and HF radar backscatter for the high-latitude ionosphere under solar minimum conditions. *Ann. Geophys.*, *29*, 377-392. doi: http://dx.doi.org/10.5194/angeo-29-377-2011

Priyadarshi, S., & Wernik, A. W. (2013). Variation of the ionospheric scintillation index with elevation angle of the transmitter. *Acta Geophysica*, *61*, 1279-1288. doi: http://dx.doi.org/10.2478/s11600-013-0123-3

Prudnikov, A. B., Brychkov, Y. A., & Marichev, O. I. (1992). *Integrals and series* (Vol. 1). CRC Press, Boca Raton.

Ratcliffe, J. A. (1956). Some aspects of diffraction theory and their application to the ionosphere. *Rep. Prog. Phys.*, *19*, 188-267. doi: http://dx.doi.org/10.1088/0034-4885/19/1/306

Rino, C. L. (1979a). A power law phase screen model for ionospheric scintillation:

1. Weak scatter. *Radio Sci.*, *14*, 1135-1145. doi: http://dx.doi.org/10.1029/RS014i006p01135

Rino, C. L. (1979b). A power law phase screen model for ionospheric scintillation: 2. Strong scatter. *Radio Sci.*, *14*, 1147-1155. doi: http://dx.doi.org/10.1029/RS014i006p01147

Rino, C. L., & Fremouw, E. J. (1977). The angle dependence of singly scattered wavefields. *J. Atm. Terr, Phys.*, *39*, 859-868. doi: http://dx.doi.org/10.1016/0021-9169(77)90166-0

Rino, C. L., Livingston, R. C., & Matthews, S. J. (1978). Evidence for sheet-like auroral ionospheric irregularities. *Geophys. Res. Lett.*, *5*, 1039-1042. doi: http://dx.doi.org/10.1029/GL005i012p01039

Rino, C. L., Livingston, R. C., Tsunoda, R. T., Robinson, R. M., Vickrey, J. F., Senior, C., ... Klobuchar, J. A. (1983). Recent studies of the structure and morphology of auroral zone F region irregularities. *Radio Sci.*, *18*, 1167-1180. doi: http://dx.doi.org/10.1029/RS018i006p01167

Rino, C. L., & Owen, J. (1980). The structure of localized nighttime auroral zone scintillation enhancements. *J. Geophys. Res.: Space Phys.*, *85*, 2941-2948. doi: http://dx.doi.org/10.1029/JA085iA06p02941

Rogers, N. C., Quegan, S., Kim, J. S., & Papathanassiou, K. P. (2014). Impacts of ionospheric scintillation on the BIOMASS P-band satellite SAR. *IEEE Trans. Geosci. and Remote Sens.*, *52*, 1856 - 1868. doi: http://dx.doi.org/10.1109/TGRS.2013.2255880

Sato, H., Kim, J. S., Otsuka, Y., Wrasse, C. M., de Paula, E. R., & de Souza, J. R. (2021). L-band synthetic aperture radar observation of ionospheric density irregularities at equatorial plasma depletion region. *Geophys. Res. Lett.*, *48*, e2021GL093541. doi: http://dx.doi.org/10.1029/2021GL093541

Secan, J. A., Bussey, R. M., Fremouw, E. J., & Basu, S. (1995). An improved model of equatorial scintillation. *Radio Sci.*, *30*, 607-617. doi: http://dx.doi.org/10.1029/94RS03172

Secan, J. A., Bussey, R. M., Fremouw, E. J., & Basu, S. (1997). High-latitude upgrade to the wideband ionospheric scintillation model. *Radio Sci.*, *32*, 1567-1574. doi: http://dx.doi.org/10.1029/97RS00453

Secan, J. A., & Fremouw, E. J. (1983). *Improvement of the scintillation-irregularity model in WBMOD* (Technical Report No. DNA-TR-81-241). Defence Nuclear Agency, Nowherecity, Washington DC.

Secan, J. A., Fremouw, E. J., & Robins, R. E. (1987). A review of recent improvements to the WBMOD ionospheric scintillation model. In J. M. Goodman, J. A. Klobuchar, R. G. Joiner, & H. Soicher (Eds.), *The effect of the ionosphere on communication, navigation, and surveillance systems* (p. 607-616). Naval Research Lab, Washington DC.

Semmling, A. M., Beckheinrich, J., Wickert, J., Beyerle, G., Schön, S., Fabra, F., ... Scheinert, M. (2014). Sea surface topography retrieved from GNSS reflectometryphase data of the GEOHALO flight mission. *Geophys. Res. Lett.*, *41*, 954-960. doi: http://dx.doi.org/0.1002/2013GL058725

Singleton, D. G. (1970). The effect of irregularity shape on radio star and satellite scintillations. *J. Atm. Terr. Phys.*, *32*, 315-343. doi: http://doi.org/10.1016/0021-9169(70)90005-X

Sinno, K., & Minakoshi, H. (1983). Experimental results on satellite scintillations due to field-aligned irregularities at mid-latitudes. *J. Atm. Terr. Phys.*, *45*, 563-567. doi: http://dx.doi.org/10.1016/S0021-9169(83)80071-3

Spencer, M. (1955). The shape of irregularities in the upper ionosphere. *Proc. Phys. Soc. B*, *68*, 493-503. doi: http://dx.doi.org/10.1088/0370-1301/68/8/302

Sunanda Basu, Basu, S., Costa, E., Bryant, C., Valladares, C. E., & Livingston, R. C. (1991). Interplanetary magnetic field control of drifts and anisotropy of high-latitude irregularities. *Radio Sci.*, *26*, 1079-1103. doi: http://dx.doi.org/

10.1029/91RS00586

Tatarski, V. I. (2016). *Wave propagation in a turbulent medium.* Dover, New York.

Tereshchenko, E. D., Khudukon, B. Z., Kozlova, M. O., , & Nygrén, T. (1999). Anisotropy of ionospheric irregularities determined from the amplitude of satellite signals at a single receiver. *Ann. Geophys.*, *17*, 508–518. doi: http://dx.doi.org/10.1007/s00585-999-0508-4

Uscinski, B. J. (1977). *The elements of wave propagation in random media.* McGraw-Hill, New York.

Vasylyev, D., Béniguel, Y., Wilken, V., Kriegel, M., & Berdermann, J. (2022). Modeling of ionospheric scintillation. *J. Space Weather Space Clim.*, *12*, 22. doi: http://dx.doi.org/10.1051/swsc/2022016

von Karman, T. (1948). Progress in the statistical theory of turbulence. *Proc. N. A. S.*, *34*, 530-539. doi: http://dx.doi.org/10.1073/pnas.34.11.530

Wang, J., & Morton, Y. T. (2017). A comparative study of ionospheric irregularity drift velocity derived from a GNSS receiver array and Poker Flat Incoherent Scatter Radar measurements during high-latitude ionospheric scintillation. *J. Geophys. Res.*, *122*, 6858-6881. doi: http://dx.doi.org/10.1002/2017JA024015

Wernik, A. W., Liu, C. H., & Yeh, K. C. (1983). Modeling of spaced-receiver scintillation measurements. *Radio Sci.*, *18*, 743-764. doi: http://dx.doi.org/10.1029/RS018i005p00743

Wild, J. P., & Roberts, J. A. (1955). The spectrum of radio-star scintillations and the nature of irregularities in the ionosphere. *J. Atm. Terr. Phys.*, *8*, 55-75. doi: http://dx.doi.org/10.1016/0021-9169(56)90091-5

Xu, Z.-W., Wu, J., & Wu, Z.-S. (2004). A survey of ionospheric effects on space-based radar. *Waves in Random Media*, *14*, S189-S2735. doi: http://dx.doi.org/10.1088/0959-7174/14/2/008

Yakovlev, O. I., Matyugov, S. S., & Vilkov, I. A. (1995). Attenuation and scintillation of radio waves in the Earth's atmosphere from radio occultation experiments on satellite-to-satellite links. *Radio Sci.*, *30*, 591-602. doi: http://dx.doi.org/10.1029/94RS01920

Yang, Z., Morton, Y. T. J., Zakharenkova, I., Cherniak, I., Song, S., & Li, W. (2020). Global view of ionospheric disturbance impactson kinematic GPS positioning solutionsduring the 2015 St. Patrick's day storm. *J. Geophys. Res.*, *125*, e2019JA027681. doi: http://dx.doi.org/10.1029/2019JA027681

Yeh, K. C., & Liu, C.-H. (1982). Radio wave scintillations in the ionosphere. *Proc. IEEE*, *70*, 324-360. doi: http://dx.doi.org/10.1109/PROC.1982.12313